AIAA JOURNAL
Vol. 48, No. 2, February 2010

Finite Difference Lattice Boltzmann Method Applied to Acoustic-Scattering Problems

E. W. S. Kam,* R. M. C. So,† S. C. Fu,‡ and R. C. K. Leung§
Hong Kong Polytechnic University, Hung Hom, Hong Kong, People's Republic of China

DOI: 10.2514/1.43753

This paper reports on an attempt to simulate acoustic waves scattering using a finite-difference lattice Boltzmann method based on an alternative lattice equilibrium particle distribution function constructed for compressible thermal fluids. The studies focus on acoustics scattering by a zero-circulation vortex and by an isolated thermal source with no heat gain/loss. Two limiting cases of each type of scattering are examined; one is the case of an incoming acoustic wave with a short wavelength, and the other has a relatively long wavelength compared with the characteristic dimension of the obstacle. These scattering problems have been treated previously using a conventional lattice Boltzmann method and a gas-kinetic scheme. The results showed that these methods were only able to simulate the short wavelength limit case with fair accuracy for the two types of acoustics scattering considered. Because the present approach is able to recover the compressible Navier–Stokes equations with correct fluid properties, the finite-difference solution of the proposed alternative modeled lattice Boltzmann equation allows the limiting cases of the acoustics scattering problems to be calculated without numerical instability. The results thus obtained are in agreement either with analysis or with results obtained from direct aeroacoustics simulations employing the compressible Navier–Stokes equations.

Nomenclature

c	=	speed of sound
c_p	=	specific heat at constant pressure
c_v	=	specific heat at constant volume
D	=	problem dimension
D_R	=	rotational degree of freedom of the particle
D_T	=	translational degree of freedom of the particle
e	=	internal energy
e_t	=	total internal energy
f	=	particle distribution function
f^{eq}	=	equilibrium particle distribution function
Kn	=	Knudsen number
$\hat{L}$	=	characteristic length
M	=	Mach number, defined in terms of reference parameters
Pr	=	Prandtl number, defined in terms of reference parameters
p	=	pressure
Re	=	Reynolds number, defined in terms of reference parameters
r	=	radial coordinate
T	=	gas temperature ($\hat{e} = \hat{c}_v \hat{T}$)
t	=	time
$\boldsymbol{u}$	=	fluid velocity vector
u	=	stream velocity component
v	=	normal velocity component
$\boldsymbol{x}$	=	position vector
x	=	stream coordinate
y	=	normal coordinate
γ	=	specific heat ratio
κ	=	fluid conductivity
λ	=	normalized acoustic wavelength (by size of vortex or thermal source)
μ	=	fluid shear viscosity
θ	=	angular position
ρ	=	fluid density
σ	=	lattice velocity magnitude
σ_d, σ_m	=	damping coefficient and damping constant
τ	=	particle collision relaxation time
ω	=	vorticity
$\boldsymbol{\xi}$	=	particle velocity vector

Subscripts

$\hat{}$	=	denotes dimensional quantities
i, j	=	vector and/or tensor indices
o	=	microscopic reference condition
r	=	macroscopic reference condition
s	=	scattered waves
v	=	vortex
w	=	incoming plane waves
α	=	index for the lattice velocity
∞	=	upstream reference condition

Received 11 February 2009; revision received 20 July 2009; accepted for publication 21 July 2009.

*Ph.D. Graduate, Mechanical Engineering Department, Corresponding author; kamwingsze@gmail.com.

†Visiting Chair Professor, Building Services Engineering, Department of Mechanical Engineering, Purdue University.

‡Ph.D. Candidate, Mechanical Engineering Department.

§Assistant Professor, Mechanical Engineering Department, Senior Member AIAA.

I. Introduction

IN THE past, direct aeroacoustics simulation (DAS) employing the Navier–Stokes (NS) equations was extremely difficult because of scale disparities in the flow and acoustics fields. Typically, aerodynamic noise has relatively small amplitude compared with flow fluctuations, that is, $p'_{\text{acous}}/p'_{\text{aero}} = 10^{-2}$ and $u'_{\text{acous}}/u'_{\text{aero}} = 10^{-3}$ where p' is the fluctuating pressure and u' is the fluctuating velocity, and the subscripts acous and aero denote the acoustic and aerodynamic field, respectively [1]. Special boundary conditions have to be formulated if the acoustic field is to be resolved correctly and the effect of reflected waves from the computational boundaries is to be minimized [2]. With the advent of computers and numerical methods, accurate resolution of the acoustics field can be accomplished through the use of a five-point, six-order finite-difference compact numerical scheme for the spatial dimension, a fourth-order Runge–Kutta scheme for time marching, and a third-order accurate treatment at the boundary to minimize wave reflection [3,4] to

numerically solve the NS equations. For ease of reference later, this numerical scheme is called the Lele scheme [3] from this point on. The Lele scheme has been used as a standard to compare with other DAS schemes for the calculation of benchmark aeroacoustics problems and duct aeroacoustics [5–7].

The simulation of scattered-plane sound waves by a zero-circulation vortex has added difficulty because in this case the amplitudes of the acoustic waves are at least 5 orders of magnitude less than the flow field [4]. Furthermore, the ratio of the incoming acoustic wavelength to the size of the vortex λ is a critical parameter that has significant effect on the scattered field. There are two λ limits in this scattering problem; a small wavelength (Wentzel–Kramers–Brillouin, or WKB) limit specified by very small to small λ, and a large wavelength (or Born) limit given by large to very large λ. Vortex scattering in these two limits has been studied by numerous researchers; in the WKB limit by Georges [8], and in the Born limit by Müller and Matschat [9], Ferziger [10], O'Shea [11], Howe [12], Candel [13], and Ford and Llewellyn Smith [14]. The scattered waves are most difficult to resolve because they are given rise by the difference between two waves. One wave is derived from the interaction between the incoming acoustic wave and the vortex, and the other is due to the undisturbed incoming wave in the absence of the vortex. In the Born limit, the scattered wave spreads out in all directions and no sharp-edged shadow is observed. On the other hand, in the WKB limit only half of the scattered wave spreads out in a near-isotropic pattern from the vortex, and the other half interacts with the incoming acoustic wave to form a sharp-edged shadow. Colonius et al. [4] were able to demonstrate that the Lele scheme is sufficiently accurate to resolve the scattering of sound waves by a vortex, especially the prediction of the directivity pattern and the far-field decay of the scattered field. The scattered features of the Born limit were well-replicated by their DAS calculations. Furthermore, their results demonstrated the inadequacies of previous vortex-scattering theories for the Born limit [11–13]. The Lele scheme has also been used in [6,7] to simulate the propagation of plane acoustic waves and Gaussian pulses, the interaction of acoustics, entropy, and vortex pulses in a uniform stream, and good agreement with analysis was obtained.

The interaction of acoustic waves with thermal sources is of common occurrence in various aerospace engineering problems and has drawn the attention of engineers and researchers. Some important examples are instability introduced by a fluctuating transfer of heat [15] and sound attenuation under favorable heat condition [16]. In spite of the important role thermal acoustic scattering plays in aerospace engineering problems, it has rarely been investigated. As a result, knowledge of the underlying physics related to thermal acoustic scattering is quite meager. On the other hand, some related studies [17–19] to this problem can be mentioned. These include the study of Trilling [17], who showed that an instantaneous temperature rise due to an infinitely long plane wall could give rise to an acoustic wave, the vortex-scattering investigation of Reinschke et al. [18], who examined the case of shock wave scattering by a hot spot, and the examination of Farouk et al. [19] on thermally induced acoustic wave in a 2-D cavity by either heating up or cooling down the vertical walls of the cavity. None of these studies deal directly with the scattering of acoustic waves by a thermal source, however.

Recently this problem was attempted by Kam et al. [20], who used patching to examine the scattering of acoustic waves by a localized thermal source with zero heat gain/loss. Again, two limiting cases were examined, a small λ or WKB limit and a large λ or Born limit. Their analysis was based on the linearized Euler equations; therefore, the interaction between the acoustic waves and the thermal disturbance was not accounted for. In an effort to resolve the thermal-acoustic interaction, Kam et al. [20] attempted to treat the nonlinear problem through a numerical investigation using the gas-kinetic scheme of Su et al. [21] and Xu and He [22] to solve the full set of compressible NS equations. It was found that the gas-kinetic scheme yields good agreement with the analytical result only for the WKB limit case. The reason for the failure of the Born limit case could be attributed to the inappropriateness of the Riemann invariant boundary conditions invoked for the gas-kinetic scheme. The Riemann invariant boundary condition works best for normal incident waves at the boundary. Because the impinging waves are no longer normal to the boundaries for the Born limit case, the nonreflecting requirement at the boundaries is no longer satisfied exactly. Consequently, reflected waves interact with incoming waves to produce unnecessary disturbances.

Attempts to use the modeled Boltzmann equation (BE) to tackle aeroacoustics problems, especially simulations employing the conventional lattice Boltzmann method (LBM) also have been made [23–26]. This is because of the simplicity of the method, which only requires the solution of a finite number of linear scalar equations compared with solving nonlinear vector and tensor equations in the gas-kinetic scheme or in DAS employing the NS equations. The LBM attempts prove to be wanting because the simulated results of benchmark aeroacoustics problems were quite often contaminated by numerical noise. There are various reasons for the rather unsatisfactory results; among them are the incorrect μ and the inability of the adopted numerical scheme to resolve the acoustics disturbances to the required accuracy. The LBM has been modified to give a correct recovery of μ [6]. Further, the Lele scheme has been adopted with slight modification and with suitable nonreflecting boundary conditions [27] to solve the modified LBM. Instead of a fourth-order Runge–Kutta time-marching scheme, the modification involved the adoption of a second-order time-marching procedure. The simulation results of benchmark aeroacoustics problems, such as the interaction of three pulses in a uniform stream, showed good agreement with DAS results obtained by solving the NS equations directly [6,7].

When this modified LBM scheme was applied to treat acoustic wave scattering by a zero-circulation vortex [28], the calculations of the WKB limit compared relatively well with DAS results obtained using the Lele scheme [3,4]. However, there were important differences between the LBM and the DAS results. These differences are 1) the directivity pattern for the root mean square density obtained from DAS is symmetric, whereas that deduced from LBM is not, 2) there is a difference in the peak value calculated from the DAS and the LBM result in the lower half plane ($\theta < 0$), and 3) the DAS result for $\theta > \pm\pi/3$ is essentially noise free, whereas that for the LBM is not. Here θ is the angular position measured positive counterclockwise from the center of the vortex. In view of this, no attempt has been made to simulate the Born limit case [28]. This suggests that the validity and extent of the modified LBM scheme for acoustic wave scattering simulation over a wide range of λ might not be comparable to those given by DAS. Further, attempts to use this modified LBM scheme to simulate the thermal-scattering problem failed to yield good agreement with analysis even for the WKB limit case [29]. It is clear that if the modeled BE were to be a viable alternative to solving the NS equations directly, further improvement of the modeled BE and possibly the associated f^{eq} is necessary.

From the brief review previously given, it is clear that the conventional or modified LBM approach needs improvement if the vortex- and thermal-scattering problem were to be successfully simulated over a wide range of λ. The objective of the present paper is to attempt an investigation of these acoustic-scattering problems using an approach based on an improved modeled lattice Boltzmann equation (LBE) with a different f^{eq}. The investigation only focuses on the WKB and the Born limit and the simulations are compared with analytical and DAS results. An attempt to improve the modeled LBE so that the Euler equations can be recovered fully has already been carried out [30,31]. In these studies, a f^{eq} that is a polynomial of $\boldsymbol{\xi}_\alpha$ instead of an expansion in terms of $\boldsymbol{\xi}_\alpha \cdot \boldsymbol{u}$ [25,32] was proposed. The modeled LBE was solved using the Lele scheme, and its simulations of aeroacoustics, 1-D, and 2-D Riemann problems gave results that were in excellent agreement with analysis up to $M_\infty \approx 1.5$. Because the vortex and the thermal disturbance are viscous [4,20], the approach of [30,31] needs to be extended to recover the NS equations fully if it is to be used to treat vortex- and thermal-scattering problems successfully. This implies that the modeled LBE has to be valid for compressible thermal fluids with μ, κ, and γ recovered correctly for an ideal gas. The extension to recover the NS equations fully with correct μ, κ, and γ has recently been attempted

Table 1 Computational details for the FDLBM and DAS simulations for vortex-scattering cases with $\lambda = 0.5$ and $\lambda = 2.5$

	FDLBM		DAS	
	$\lambda = 0.5$	$\lambda = 2.5$	$\lambda = 0.5$	$\lambda = 2.5$
Grid size	$\Delta x = \Delta y = 2.5 \times 10^{-2}$	$\Delta x = \Delta y = 5 \times 10^{-2}$	$\Delta x = \Delta y = 2.5 \times 10^{-2}$	$\Delta x = \Delta y = 5 \times 10^{-2}$
Spatial discretization scheme	6th-order compact scheme		6th-order compact scheme	
Time step	$\Delta t = 0.0001$		$\Delta t = 0.01$	
Physical domain size	$-3.0 \le x \le 2.5$	$-8.75 \le x \le 6.25$	$-3.0 \le x \le 2.5$	$-8.75 \le x \le 6.25$
	$-2.5 \le y \le 2.5$	$-6.25 \le y \le 6.25$	$-2.5 \le y \le 2.5$	$-6.25 \le y \le 6.25$
No. of grid points	260, 200	340, 250	300, 200	380, 250
Absorbing boundary conditions	20 points for inlet (D_I) and outlet (D_O); $\sigma_m = 10$		40 points for inlet (D_I) and outlet (D_O); $\sigma_m = 10$	
Upper and lower boundaries	Zero-order extrapolation for f		Zero-order extrapolation for u, v, p, T	
Location of incoming wave	$x = -3.0$	$x = -8.75$	$x = -3.0$	$x = -8.75$
$M_\infty/Re_\infty = \hat{\mu}_\infty/\hat{\rho}_\infty\hat{c}_\infty\hat{L}$	2×10^{-4}		2×10^{-4}	
Pr_∞	0.71		0.71	
Wall clock running time	439 min	599 min	38 min	139 min

Table 2 Computational details for the FDLBM and theoretical simulations for $\lambda = 1/3$ and $\lambda = 10/3$ thermal-scattering cases

	FDLBM	Analysis
Grid sizes	$\Delta x = \Delta y = 5 \times 10^{-2}/3$	$\Delta x = \Delta y = 5 \times 10^{-2}/3$
Spatial discretization scheme	6th-order compact scheme	——
Time step	$\Delta t = 0.0001$	——
Time-marching	2nd-order Runge–Kutta scheme	——
Physical domain size for the $\lambda = 1/3$ case	$-10.0/3 \le x \le 10.0/3$	$-10.0/3 \le x \le 10.0/3$
	$-10.0/3 \le y \le 10.0/3$	$-10.0/3 \le y \le 10.0/3$
'Physical domain size for the $\lambda = 10/3$ case	$-100.0/3 \le x \le 100.0/3$	$-100.0/3 \le x \le 100.0/3$
	$-100.0/3 \le y \le 100.0/3$	$-100.0/3 \le y \le 100.0/3$
No. of grid points	440, 400	440, 400
Absorbing boundary conditions	20 points for inlet (D_I) and outlet (D_O); $\sigma_m = 10$	——
Upper and lower boundaries	Zero-order extrapolation for f	——
Location of incoming wave for $\lambda = 1/3$ case	$x = -10.0/3$	$x = -10.0/3$
Location of incoming wave for $\lambda = 10/3$ case	$x = -100.0/3$	$x = -100.0/3$
$M_\infty/Re_\infty = \hat{\mu}_\infty/\hat{\rho}_\infty\hat{c}_\infty\hat{L}$	2×10^{-4}	——
Pr_∞	0.71	——
Wall clock running time	3402 min	2454 min

by So et al. [33]. They extended the f^{eq} of [30,31] to viscous compressible flows, and proposed an alternate finite difference method to solve the LBE (hereafter their method, also adopted in this paper, is designated as FDLBM). Their aeroacoustics and shock structure simulations were compared with DAS and analytical results; excellent agreement was obtained. In view of the success of the FDLBM for viscous compressible flows with shocks, it is appropriate to attempt an assessment of the validity and extent of the FDLBM against acoustic-scattering problems in the present paper, thus allowing a wider range of applicability of the FDLBM to be established. If this were proven viable, the suitability of the proposed FDLBM for a wide range of aeroacoustics and aerodynamic problems can be demonstrated. The FDLBM and its numerical solution have been described in detail in [33]; however, for the sake of completeness a brief outline is provided here. This is followed by a discussion of the vortex- and thermal-scattering results.

II. Modeled Lattice Boltzmann Equation

The following derivation parallels that given in [30,33] for the recovery of the Euler and the NS equations with correct μ, κ, and γ. The starting point is the velocity space discretized form of the Bhatnagar–Gross–Krook (BGK)-type modeled LBE [34],

$$\frac{\partial f_\alpha}{\partial t} + \boldsymbol{\xi}_\alpha \cdot \nabla_x f_\alpha = -\frac{1}{\tau Kn}(f_\alpha - f_\alpha^{\text{eq}}) \tag{1}$$

This equation is made dimensionless using the normalizations given by $\tau = \hat{\tau}/\hat{\tau}_o$, $\boldsymbol{\xi} = \hat{\boldsymbol{\xi}}/\hat{c}_\infty$, $Kn = \hat{x}_o/\hat{L}$, $(f, f^{\text{eq}}) = (\hat{f}, \hat{f}^{\text{eq}})/(\hat{\rho}_\infty/\hat{c}_\infty^D)$, $\hat{\tau}_o = \hat{L}Kn/\hat{c}_\infty$. Here, the hat is used to designate dimensional quantities. It is necessary to demonstrate that Eq. (1) can be used to recover the NS equations exactly. To carry this out, f_α^{eq} needs to be known and so does the method used to solve Eq. (1). In what follows,

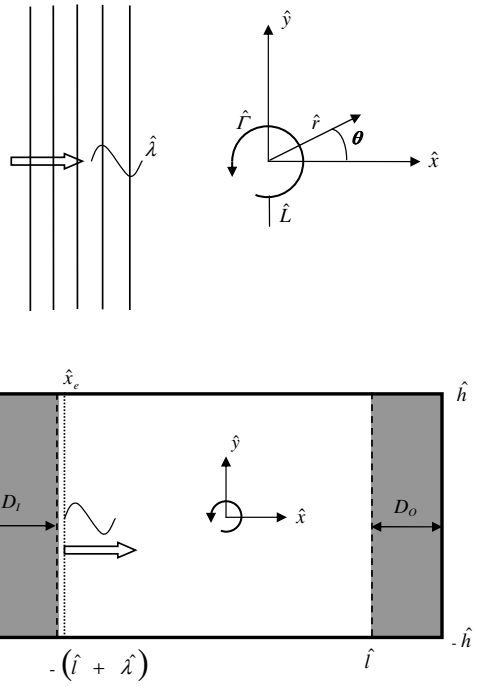

Fig. 1 Problem definition of acoustics waves scattering by a zero-circulation vortex: a) schematic of problem, and b) computational domain and buffer layers.

a different f_α^{eq} and an appropriate velocity lattice model are used to seek solution to Eq. (1), and then the recovery of the NS equations is demonstrated. Finally, the determination of the coefficients in the proposed f_α^{eq} is described.

A. Velocity Lattice Model and f_α^{eq}

Because only 2-D flows are considered in this paper, the modeled LBE in a 2-D domain is given. The 3-D counterpart can be easily obtained by following the same procedure. Under the BGK-type model, the deviation of f from f^{eq} is assumed small; hence, a Chapman–Enskog expansion of f_α in terms of Kn can be written as

$$f_\alpha = f_\alpha^{(0)} + Kn f_\alpha^{(1)} + Kn^2 f_\alpha^{(2)} + \mathcal{O}(Kn^3) \tag{2}$$

The equations for $f^{(1)}$, $f^{(2)}$, and so forth can be obtained by substituting Eq. (2) into Eq. (1) and collecting terms with the same order of Kn. It can be shown that, to zero order of Kn, $f_\alpha^{(0)} = f_\alpha^{\mathrm{eq}}$, and the first-order equation after substituting $f_\alpha^{(0)}$ by f_α^{eq} is given by

$$\frac{\partial f_\alpha^{\mathrm{eq}}}{\partial t} + \boldsymbol{\xi}_\alpha \cdot \nabla_x f_\alpha^{\mathrm{eq}} = -\frac{f_\alpha^{(1)}}{\tau} \tag{3}$$

In the present approach, only the first-order equation is used to recover the NS equations (see derivation to follow); therefore, the higher-order equations are not shown.

A two-dimensional, nine-velocity lattice model (D2Q9) has been found to be sufficient for accurate resolution of all aeroacoustics and shock-capturing problems considered [30,31]. In view of this, the current formulation again relies on the use of a D2Q9 model. For a D2Q9 model, the lattice velocity is given by

$$\boldsymbol{\xi}_0 = 0, \qquad \alpha = 0 \tag{4a}$$

$$\boldsymbol{\xi}_0 = \sigma\{\cos[\pi(\alpha-1)/4], \sin[\pi(\alpha-1)/4]\}, \qquad \alpha = 1,3,5,7 \tag{4b}$$

$$\boldsymbol{\xi}_\alpha = \sqrt{2}\sigma\{\cos[\pi(\alpha-1)/4], \sin[\pi(\alpha-1)/4]\}, \qquad \alpha = 2,4,6,8 \tag{4c}$$

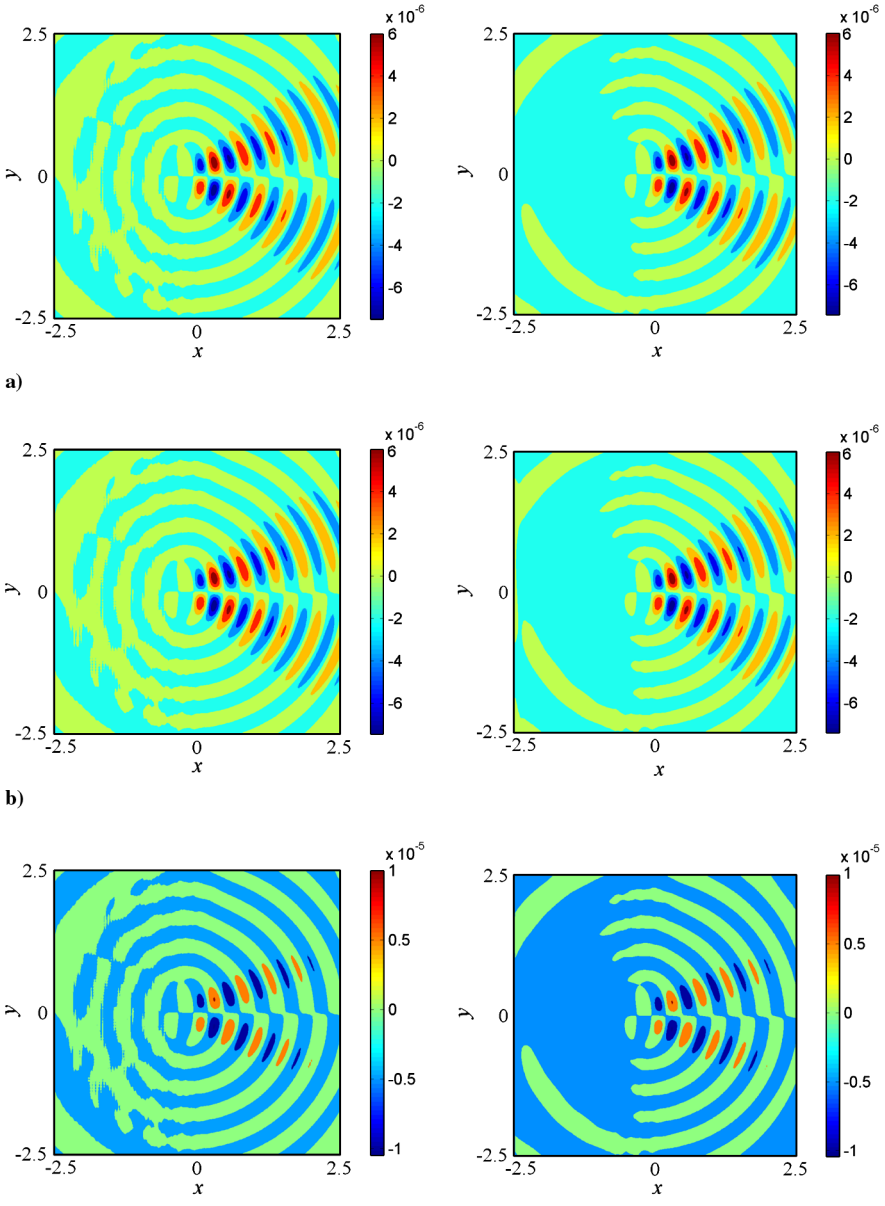

Fig. 2 2-D contours of a) p_s, b) ρ_s, and c) T_s for the $\lambda = 0.5$ vortex-scattering case. The left-hand column represents FDLBM, and the right-hand column represents DAS.

where σ represents the magnitude of the velocity lattice and needs to be determined.

Just as in the case of the recovery of the Euler equations [30,31], a polynomial series in $\boldsymbol{\xi}_\alpha$ up to second order is proposed for the discretized form of f_α^{eq}, that is,

$$f_\alpha^{\mathrm{eq}} = A_\alpha + \xi_{\alpha x} A x_\alpha + \xi_{\alpha y} A y_\alpha + \xi_{\alpha x}^2 B x x_\alpha + \xi_{\alpha y}^2 B y y_\alpha + \xi_{\alpha x}\xi_{\alpha y} B x y_\alpha \tag{5}$$

Here, the indices x and y are used to denote the stream and cross-stream direction in a 2-D flow, and the coefficients A_α, Ax_α, Bxx_α, and so forth are components of scalars, vectors, or tensors. These coefficients are not known and need to be determined. Their determination is described in [30,33]. However, it is not necessary to know these coefficients a priori in recovering the NS equations. Consequently, the determination of these coefficients is outlined after the NS equations' recovery has been demonstrated. It should be pointed out that Eq. (5) is a polynomial expressed in terms of $\boldsymbol{\xi}_\alpha$ and is not an expansion in terms of $\boldsymbol{\xi}_\alpha \cdot \boldsymbol{u}$ [25,32]. It is anticipated that viscous and thermal effect will enter into the coefficients A_α, Ax_α, Bxx_α, and so forth; therefore, the resulting f_α^{eq} will be different from those derived in [30,31]. For compressible flows with large temperature or density gradient the proposed Eq. (5) for f_α^{eq} might not be adequate; in those cases a polynomial with more terms to account for heat transfer during the collision process might be necessary.

B. Recovery of the NS Equations

The recovery of the NS equations from Eq. (1) follows the procedure laid out in [30] and adopted in [33]. First, it is assumed that for each α, f_α can be expanded in terms of Kn as given in Eq. (2), such that the macroconstraints of density ρ, linear momentum $\rho\boldsymbol{u}$, and total internal energy e_t are satisfied. In addition, the momentum and energy equation of the NS equations are used to derive additional constraints to help determine the coefficients in Eq. (5). For 2-D flows these constraints, written in Cartesian coordinates, are given by (with $N = 8$ for a D2Q9 model)

$$\sum_{\alpha=0}^{N} f_\alpha^{\mathrm{eq}} = \rho \tag{6a}$$

$$\sum_{\alpha=0}^{N} f_\alpha^{\mathrm{eq}} \xi_{\alpha x} = \rho u \tag{6b}$$

$$\sum_{\alpha=0}^{N} f_\alpha^{\mathrm{eq}} \xi_{\alpha y} = \rho v \tag{6c}$$

$$\sum_{\alpha=0}^{N} f_\alpha^{\mathrm{eq}} (\xi_{\alpha x}^2 + \xi_{\alpha y}^2) = \frac{4}{\mathrm{D}_T + \mathrm{D}_R} (\rho e_t) \tag{6d}$$

$$\sum_{\alpha=0}^{N} f_\alpha^{\mathrm{eq}} \xi_{\alpha x}^2 = \rho u^2 + p + \tau_{xx} + P'_{xx} \tag{7a}$$

$$\sum_{\alpha=0}^{N} f_\alpha^{\mathrm{eq}} \xi_{\alpha y}^2 = \rho v^2 + p + \tau_{yy} + P'_{yy} \tag{7b}$$

$$\sum_{\alpha=0}^{N} f_\alpha^{\mathrm{eq}} \xi_{\alpha x}\xi_{\alpha y} = \rho u v + \tau_{xy} + P'_{xy} \tag{7c}$$

$$\sum_{\alpha=0}^{N} f_\alpha^{\mathrm{eq}} (\xi_{\alpha x}^2 + \xi_{\alpha y}^2)\xi_{\alpha x} = \frac{4}{\mathrm{D}_T + \mathrm{D}_R} [u(\rho e_t) + u\tau_{xx} + v\tau_{xy} + q_x] \tag{8a}$$

$$\sum_{\alpha=0}^{N} f_\alpha^{\mathrm{eq}} (\xi_{\alpha x}^2 + \xi_{\alpha y}^2)\xi_{\alpha y} = \frac{4}{\mathrm{D}_T + \mathrm{D}_R} [v(\rho e_t) + u\tau_{xy} + v\tau_{yy} + q_y] \tag{8b}$$

$$\sum_{\alpha=0}^{N} f_\alpha^{(n)} = 0 \quad \text{for } n \geq 1 \tag{9a}$$

$$\sum_{\alpha=0}^{N} f_\alpha^{(n)} \xi_{\alpha x} = 0 \quad \text{for } n \geq 1 \tag{9b}$$

$$\sum_{\alpha=0}^{N} f_\alpha^{(n)} \xi_{\alpha y} = 0 \quad \text{for } n \geq 1 \tag{9c}$$

$$\frac{\mathrm{D}_T + \mathrm{D}_R}{4} \sum_{\alpha=0}^{N} f_\alpha^{(n)} (\xi_{\alpha x}^2 + \xi_{\alpha y}^2) = 0 \quad \text{for } n \geq 1 \tag{9d}$$

The first group defined in Eqs. (6a–6d) is derived from the macroproperties, the second group given by Eqs. (7a–7c) is obtained from the normalized momentum equation, and the third group

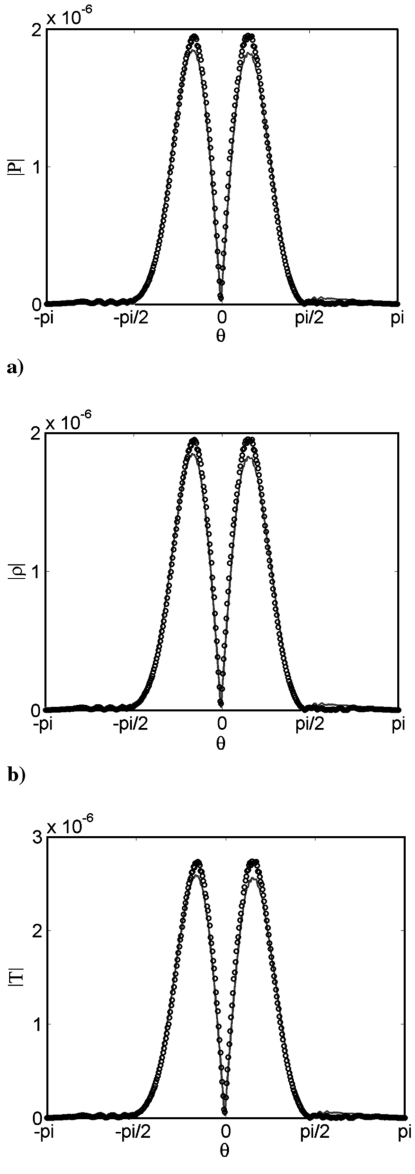

Fig. 3 Scattered distributions of a) p_s, b) ρ_s, and c) T_s, at $\hat{r}/\hat{\lambda} = 5$ for the $\lambda = 0.5$ vortex-scattering case. The circles represent FDLBM, and the solid line represents DAS.

represented by Eqs. (8a) and (8b) is deduced from the dimensionless energy equation. The last group given by Eqs. (9a–9d) simply states that summation of all $f_\alpha^{(n)}$ and their moments vanish for $n \geq 1$. In these equations,

$$-\tau_{ij} = \frac{M_\infty}{Re_\infty} 2\mu \left(S_{ij} - \frac{1}{3}\delta_{ij} S_{kk} \right) \tag{10a}$$

$$q_j = -\frac{\gamma M_\infty}{Re_\infty Pr_\infty} \left(\kappa \frac{\partial e}{\partial x_j} \right) \tag{10b}$$

have been substituted and all terms are normalized using the same characteristic scaling as those invoked for Eq. (1). In addition, the scaling $\hat{c}_\infty$ is used for the macrovelocity $\hat{\boldsymbol{u}}$, $\hat{\rho}_\infty \hat{c}_\infty^2$ for pressure, $\hat{c}_\infty^2$ for energy, $\hat{\mu}_\infty$ for viscosity, and $\hat{\kappa}_\infty$ for conductivity. Therefore, $M_\infty = \hat{U}_\infty / \hat{c}_\infty$, $Re_\infty = \hat{\rho}_\infty \hat{L} \hat{U}_\infty / \hat{\mu}_\infty$, $Pr_\infty = \hat{\mu}_\infty (\hat{c}_p)_\infty / \hat{\kappa}_\infty$, $\mu = \hat{\mu} / \hat{\mu}_\infty$, $\kappa = \hat{\kappa} / \hat{\kappa}_\infty$, and $\hat{U}_\infty$ is the reference mean flow velocity. The strain tensor S_{ij} is given by $S_{ij} = \{(\partial u_i / \partial x_j) + (\partial u_j / \partial x_i)\}/2$. The tensor P'_{ij} in Eqs. (7a–7c) has to satisfy the divergence condition for P'_{ij}, that is,

$$\frac{\partial P'_{ij}}{\partial x_j} = 0 \tag{11}$$

Otherwise, the momentum equation cannot be recovered correctly. These relations not only allow the macroproperties to be evaluated, they also stipulate that the NS equations should be recovered correctly.

Secondly, multiplying Eq. (3) with respect to $\{1, \boldsymbol{\xi}_\alpha, (|\boldsymbol{\xi}_\alpha|^2)(\mathrm{D}_T + \mathrm{D}_R)/4\}^T$ and taking summation over α, then substituting Eq. (2) into these resulting equations and making use of the relations given in Eqs. (6–9), the final macrotransport equations for a 2-D flow in Cartesian coordinates are obtained

$$\frac{\partial \rho}{\partial t} + \frac{\partial \rho u}{\partial x} + \frac{\partial \rho v}{\partial y} + \mathcal{O}(Kn) = 0 \tag{12a}$$

$$\frac{\partial (\rho u)}{\partial t} + \frac{\partial}{\partial x}(\rho u^2 + p + \tau_{xx} + P'_{xx}) + \frac{\partial}{\partial y}(\rho u v + \tau_{xy} + P'_{xy}) + \mathcal{O}(Kn) = 0 \tag{12b}$$

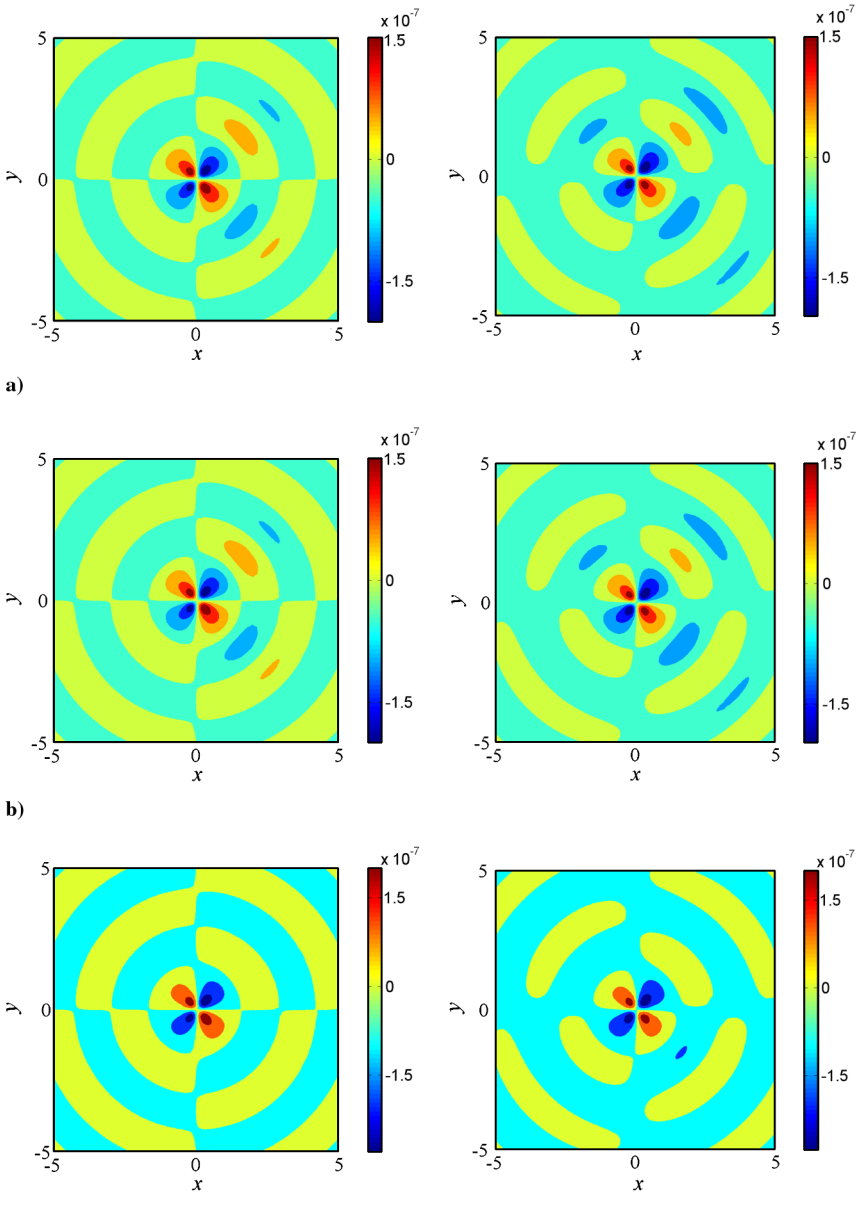

Fig. 4 2-D contour of a) p_s, b) ρ_s, and c) T_s for the $\lambda = 2.5$ vortex-scattering case. The left-hand column represents FDLBM, and the right-hand column represents DAS.

$$\frac{\partial(\rho v)}{\partial t}+\frac{\partial}{\partial x}(\rho uv+\tau_{xy}+P'_{xy}) + \frac{\partial}{\partial y}(\rho v^2+p+\tau_{yy}+P'_{yy})+\mathcal{O}(Kn)=0 \quad (12c)$$

$$\frac{\partial(\rho e_t)}{\partial t}+\frac{\partial}{\partial x}[u(\rho e_t+p)+u\tau_{xx}+v\tau_{xy}+q_x] + \frac{\partial}{\partial y}[v(\rho e_t+p)+u\tau_{xy}+v\tau_{yy}+q_y]+\mathcal{O}(Kn)=0 \quad (12d)$$

where the ideal gas equation of state, $p=\rho e(\gamma-1)$, has been invoked. Therefore, the NS equations for a continuum fluid normalized using acoustic scaling is recovered [35] provided that Eq. (11), which can be easily derived from Eqs. (12b) and (12c), is satisfied. This implies that Eq. (11) has to be solved simultaneously with Eq. (1). As has been shown in [32], the solution of Eq. (11) does not unduly complicate the finite difference solution of Eq. (1); numerical details of solving Eq. (1) are given in the next section.

C. Determination of the Coefficients of f_α^{eq}

Of the nine equations within Eqs. (6–8), only eight are independent because one is a duplicate of the kinetic energy equation. These equations are used to evaluate A_α, Ax_α, Bxx_α, etc. If the coefficients having the same energy shell of the lattice velocities are assumed to be the same, the number of unknowns resulting from the coefficients A_α, Ax_α, Bxx_α, and so forth, are 13 in a D2Q9 lattice model. Because the number of constraints available for the determination of these coefficients is 8, there is certain flexibility and assumptions can be made to facilitate solution of the equations. As a first attempt, five coefficients (A_1, A_2, Bxx_2, Byy_2, and Bxy_1) out of the 13 are assumed zero; the choice of these coefficients is guided by the need to recast Eq. (5) in a form similar to those given in [25,32]. Details of this derivation are given in [30] for the Euler equations and in [33] for the NS equations. The present analysis follows this derivation procedure and the results are

$$A_0=\rho-\frac{2p}{\sigma^2}-(\gamma-1)\frac{\rho|\boldsymbol{u}|^2}{\sigma^2}, \qquad A_1=A_2=0 \quad (13a)$$

$$Ax_1=\frac{\rho u}{\sigma^2}-\frac{\gamma p u}{\sigma^4}-(\gamma-1)\frac{1}{2}\frac{\rho|\boldsymbol{u}|^2u}{\sigma^4}-(\gamma-1)\frac{q_x+u\tau_{xx}+v\tau_{xy}}{\sigma^4} \quad (13b)$$

$$Ax_2=-\frac{1}{4}\frac{\rho u}{\sigma^2}+\frac{1}{2}\frac{\gamma p u}{\sigma^4}+(\gamma-1)\frac{1}{4}\frac{\rho|\boldsymbol{u}|^2u}{\sigma^4} + (\gamma-1)\frac{q_x+u\tau_{xx}+v\tau_{xy}}{2\sigma^4} \quad (13c)$$

$$Ay_1=\frac{\rho v}{\sigma^2}-\frac{\gamma p v}{\sigma^4}-(\gamma-1)\frac{1}{2}\frac{\rho|\boldsymbol{u}|^2v}{\sigma^4}-(\gamma-1)\frac{q_x+u\tau_{xy}+v\tau_{yy}}{\sigma^4} \quad (13d)$$

$$Ay_2=-\frac{1}{4}\frac{\rho v}{\sigma^2}+\frac{1}{2}\frac{\gamma p v}{\sigma^4}+(\gamma-1)\frac{1}{4}\frac{\rho|\boldsymbol{u}|^2v}{\sigma^4} + (\gamma-1)\frac{q_y+u\tau_{xy}+v\tau_{yy}}{2\sigma^4} \quad (13e)$$

$$Bxx_1=\frac{1}{2\sigma^4}(p+\rho u^2+\tau_{xx}+P'_{xx}), \qquad Bxx_2=0 \quad (13f)$$

$$Byy_1=\frac{1}{2\sigma^4}(p+\rho v^2+\tau_{yy}+P'_{yy}), \qquad Byy_2=0 \quad (13g)$$

$$Bxy_2=\frac{1}{4\sigma^4}(\rho uv+\tau_{xy}+P'_{xy}), \qquad Bxy_1=0 \quad (13h)$$

Up to this point, all parameters and coefficients in Eq. (5) are known except σ. Therefore, once σ is determined there are no arbitrary constants in the formulation, not even τ (determination of τ can be found in the next section). This unique property distinguishes the present approach from the conventional LBM. The bounds for σ can be determined by first considering Eq. (6d), from which the following expression can be deduced

$$\min(|\boldsymbol{\xi}_\alpha|^2)\sum_{\alpha=0}^{N}f_\alpha^{eq}\le\frac{4}{D_T+D_R}\left(\rho e+\frac{1}{2}\rho|\boldsymbol{u}|^2\right) \le\max(|\boldsymbol{\xi}_\alpha|^2)\sum_{\alpha=0}^{N}f_\alpha^{eq} \quad (14)$$

Thus, using $\sigma^2=|\boldsymbol{\xi}_\alpha|^2$ deduced from Eq. (4b) and (14), the value of σ can be estimated. As such, there are no arbitrary constants in Eq. (5); however, P'_{xy}, P'_{xx}, and P'_{yy} are still not known. These unknowns are governed by Eq. (11). As shown in [30], a possible solution set for Eq. (11) can be written for an infinite domain; for other types of domain, Eq. (11) has to be solved numerically. The numerical solution of Eq. (11) follows closely the methodology details in [33]. Once P'_{xy}, P'_{xx}, and P'_{yy} are known, Eqs. (13a–13h) can be determined and the solution of Eq. (1) follows in a straightforward manner.

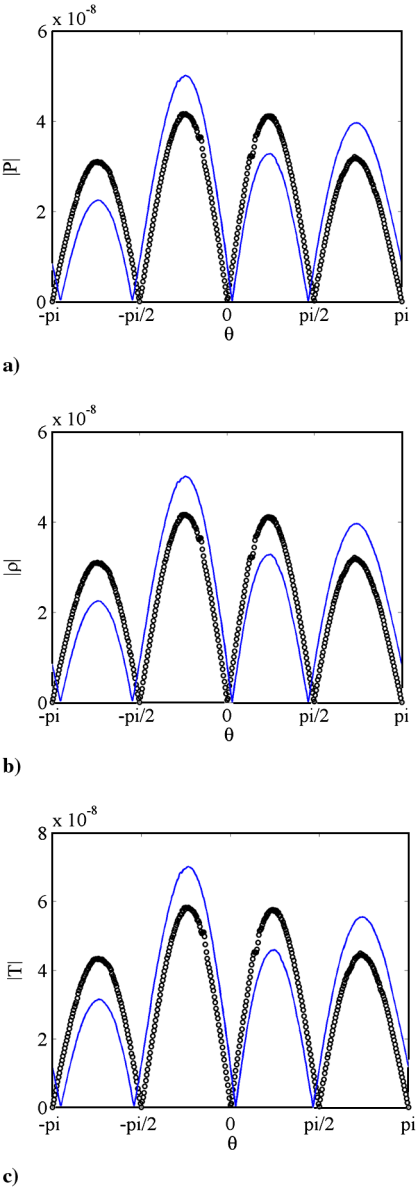

Fig. 5 Distribution of a) p_s, b) ρ_s, and c) T_s at $\hat{r}/\hat{\lambda}=2$ for the $\lambda=2.5$ vortex-scattering case. The patterned line represents FDLBM, and the solid line represents DAS.

III. Finite Difference Lattice Boltzmann Method

In principle, Eq. (1) can be used to resolve aerodynamic disturbances by adopting any standard finite difference scheme because it can be viewed as a system of inhomogeneous hyperbolic equations. However, certain difficulties in aeroacoustics simulation are not present in numerical studies of aerodynamic problems. Some of these difficulties are 1) aeroacoustic disturbances are typically at least 2 orders of magnitude smaller than aerodynamic disturbances, 2) disparity of scales in aeroacoustics put a heavy burden on numerical accuracy, and 3) the computational boundaries have to be totally nonreflecting, or the reflected waves will interact with the incoming and outgoing waves to give rise to additional disturbances that are not part of the solution. In addition, using Eq. (1) to simulate aeroacoustic disturbances introduces another difficulty not found in solving the NS equations directly. This is the necessity of having to specify the boundary value of f_α at every time step. It is no easy task to set a proper boundary condition for f_α because, for any physical boundary condition stipulated for macroscopic quantities, it is sometimes difficult to find a corresponding f_α, and the traditional bounce-back wall boundary condition is not quite suitable. In view of this, only finite difference schemes with certain properties can be used to solve Eq. (1). Therefore, a suitable finite difference scheme for Eq. (1) should have high spatial resolution, accurate time marching, and most importantly would allow the setting of boundary condition for f_α to be as easy as its counterpart in solving the NS equations directly [4]. The scheme described in the following section has all these attributes and is designated as FDLBM.

Traditional LBM is only second-order accurate in both spatial and temporal dimensions; thus, it is not accurate enough for aeroacoustics simulations. In view of the development of the Lele scheme [4], it is also adopted here to treat Eq. (1). This scheme is further improved to allow the boundary condition for f_α to be specified as freely as any conventional finite difference scheme for the solution of the NS equations. To achieve this objective, it is proposed to solve Eq. (1) using a splitting technique, which is a common approach for solving partial differential equations with source terms [36]. Consequently, Eq. (1) is solved in three steps.

1) Initialization step where the initial conditions of all macroscopic quantities are used to calculate the initial equilibrium distribution function, $f_\alpha^{o,\mathrm{eq}}$, using Eqs. (5) and (13). Thus determined, $f_\alpha^{o,\mathrm{eq}}$

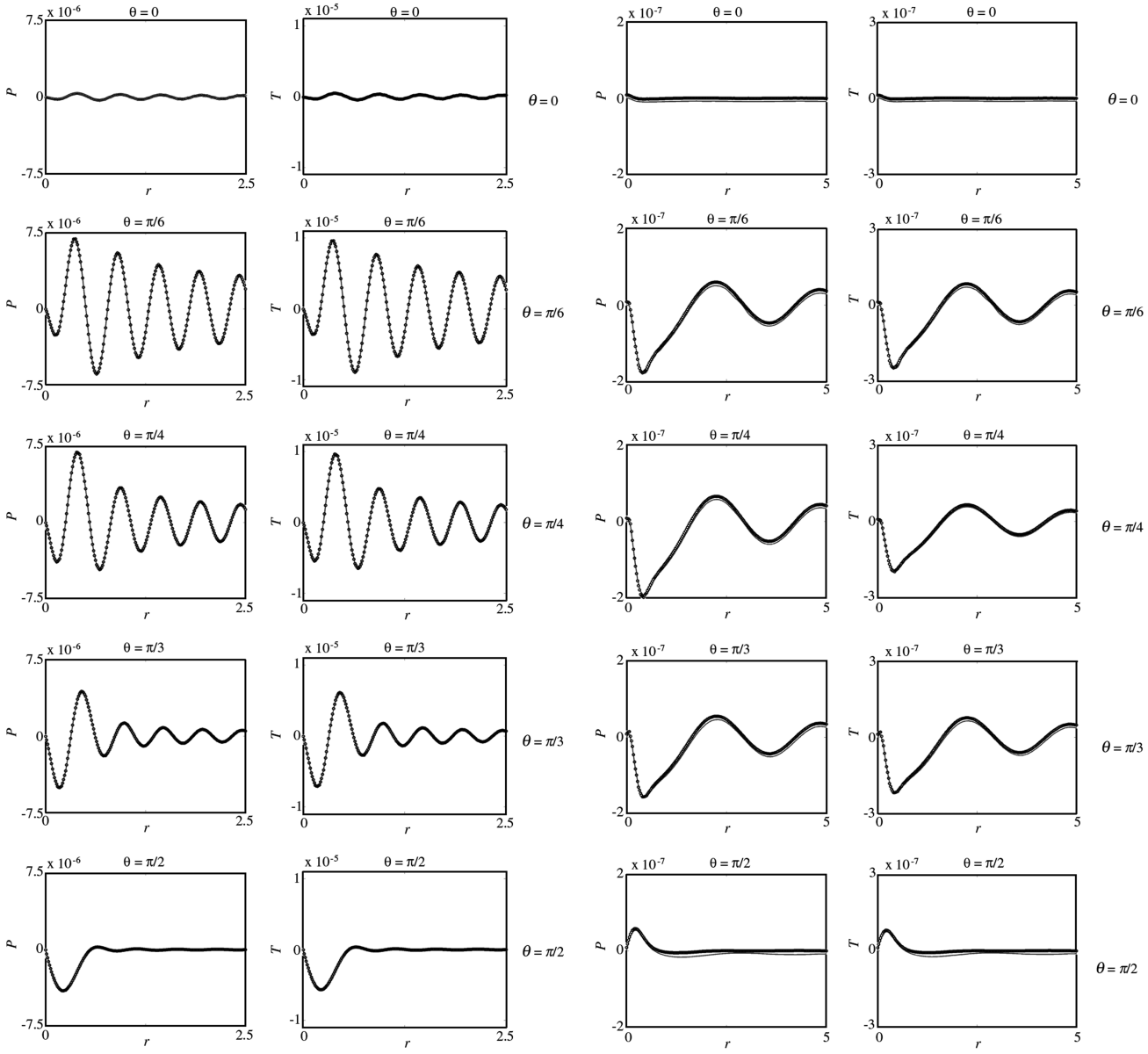

Fig. 6 Distribution along r of (left-hand column) p_s and (right-hand column) T_s at different θ for a) $\lambda = 0.5$ case and b) $\lambda = 2.5$ case. In both cases, the patterned line represents FDLBM, and the solid line represents DAS.

(including the boundary points) is used to start the calculation in the streaming step.

2) Streaming step where the homogenous hyperbolic equation,

$$\frac{\partial f_\alpha}{\partial t} + \boldsymbol{\xi}_\alpha \cdot \nabla_x f_\alpha = 0 \tag{15}$$

is solved. Once f_α at time t (including the boundary points) is known, a second-order Runge–Kutta time-marching scheme is used to evaluate the time-dependent term in Eq. (15) and a compact sixth-order finite difference scheme is adopted for the calculation of the convection term in Eq. (15). This procedure is only applied to the interior grid points in the domain. The result gives the intermediate value, f_α^I (excluding boundary points). Once this f_α^I is known, the intermediate macroscopic quantities (ρ_I, u_I, v_I, p_I) for all interior grid points are calculated from Eqs. (6–9) and the boundary conditions for the macroscopic level are then set. Finally, using these macroscopic quantities (complete domain including the boundary points) and invoking Eqs. (5) and (13), the intermediate equilibrium distribution function $f_\alpha^{I,\mathrm{eq}}$ is obtained (including all boundary points). This $f_\alpha^{I,\mathrm{eq}}$ could be different from f_α^I determined previously.

3) Collision step where the results obtained in step 2 provide the necessary initial conditions for the solution of the equation

$$\frac{\partial f_\alpha}{\partial t} = -\frac{1}{\tau Kn}(f_\alpha - f_\alpha^{\mathrm{eq}}) \tag{16a}$$

The Euler method with the choice $\Delta t = \tau Kn$ is used to discretize Eq. (16a), thus giving

$$\frac{f_\alpha(\boldsymbol{x}, t+\Delta t) - f_\alpha(\boldsymbol{x}, t)}{\Delta t} = -\frac{1}{\tau Kn}[f_\alpha(\boldsymbol{x}, t) - f_\alpha^{\mathrm{eq}}(\boldsymbol{x}, t)]$$
$$\Rightarrow f_\alpha(\boldsymbol{x}, t+\Delta t) = f_\alpha^{\mathrm{eq}}(\boldsymbol{x}, t) \tag{16b}$$

The collision step is completed by exactly setting the new f_α (at time $t + \Delta t$) as the equilibrium distribution function $f_\alpha^{I,\mathrm{eq}}$. Because each set of macroscopic quantities will map uniquely to an equilibrium distribution function, and vice versa, the macroscopic quantities thus obtained are the values at time $(t + \Delta t)$, that is, $(\rho, u, v, p)|_{t+\Delta t} = (\rho_I, u_I, v_I, p_I)$.

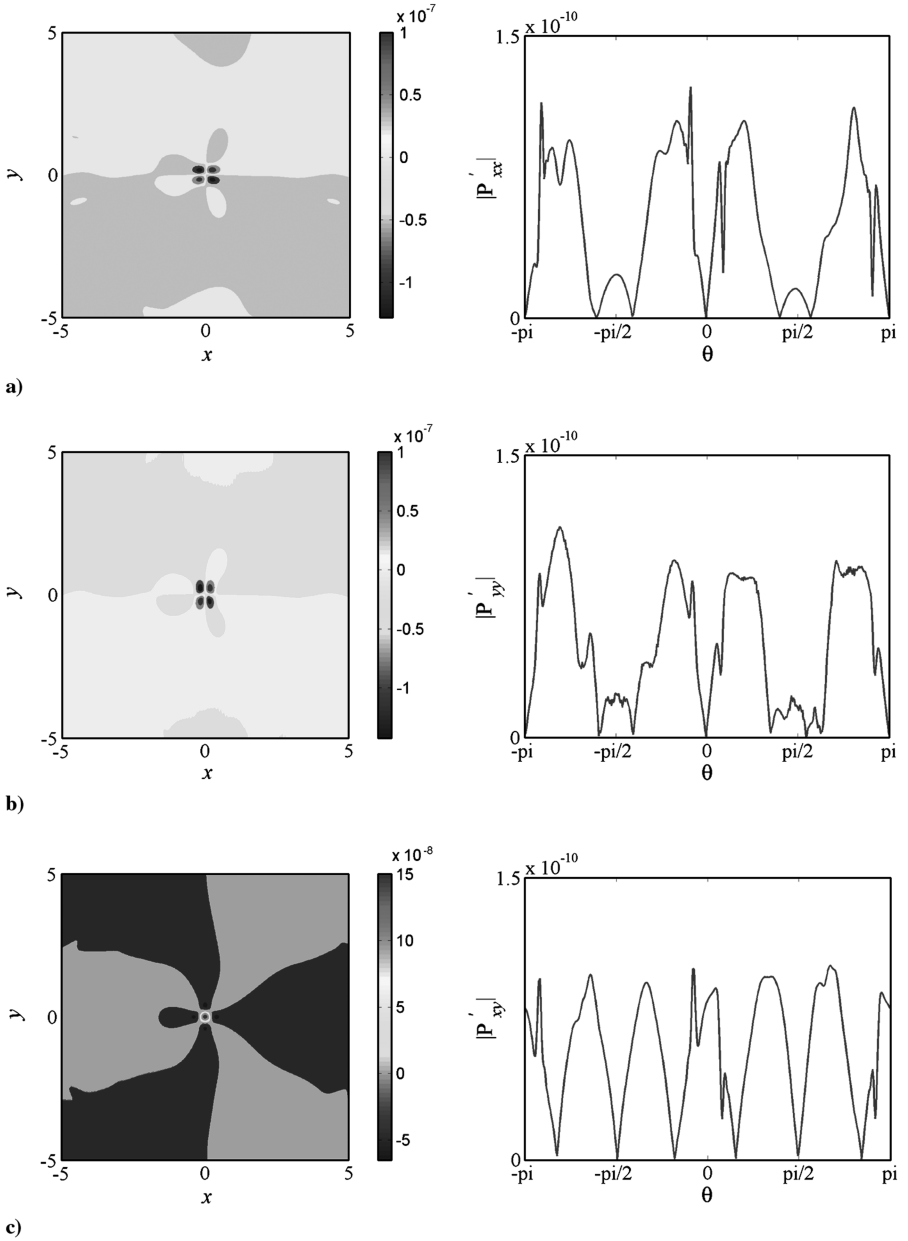

Fig. 7 The FDLBM simulated scattered field of P'_{ij} for the $\lambda = 2.5$ vortex-scattering case: a) P'_{xx}, b) P'_{yy}, and c) P'_{xy}. The left-hand column represents 2-D contour, and the right-hand column represents directivity at $\hat{r}/\hat{\lambda} = 2$.

The calculation is time-marched forward by repeating procedures 2 and 3. Further details of this FDLBM scheme can be found in [33,37].

The solution of Eq. (11) can be briefly described as follows. Again, details are given in [33]. Individual elements of P'_{ij} can be obtained by solving Eq. (11) and the trace of P'_{ij} given by the relation $\sum P'_{kk} = A$, where

$$A = [\{2 - (D_T + D_R)\}/(D_T + D_R)]\rho|\boldsymbol{u}|^2 - \sum \tau_{kk}$$

It can be shown that three Poisson equations, one for each of the three independent elements of P'_{ij}, can be derived from Eq. (11) and $\sum P'_{kk} = A$. In solving the Poisson equation for P'_{xy}, Neumann condition is assumed for the top and bottom boundary, and Dirichlet condition is invoked for the left and right boundary. On the other hand, Neumann condition is assumed for the left and right boundary and Dirichlet condition is used for the top and bottom boundary in the solution of the Poisson equation for P'_{kk}. Once these elements are known, they allow the coefficients Bxx_1, Byy_1, and Bxy_2 to be determined correctly.

Up to this point, the relaxation time τ in Eq. (1) or (16) has not been specified; it can be estimated as follows. The term τKn always appears together in Eq. (1) and (16), thus implying that τ and Kn need not be specified separately. Because Kn is of the order of 10^{-7} according to [38], the term τKn would be much smaller than one when compared with other terms in Eq. (1). This is the case even if τ is of an order greater than one. In the present calculation, $\Delta t = \tau Kn = 10^{-4}$ is chosen and this is sufficient to give results identical to those obtained with DAS. Furthermore, numerical instability was not encountered even without using high-order filters.

An absorbing boundary condition with a damping coefficient given by

$$\sigma_d = \sigma_m(\delta/D_d)^2$$

where σ_m is a constant to be specified, δ is the distance measured from the start of the damping region, and D_d is its width, has been used with success in [27]. In that study, it was found that a choice of $D_d = 1$ gave reliable and accurate results compared with those obtained from DAS calculations [27]. The choice of σ_m varies from problem to problem and, quite often, σ_m is determined by trial and error for each problem. In the present study, the same damping coefficient with $\sigma_m = 10$ is adopted. This value of σ_m was found to give the best results for all four cases examined. Furthermore, a D2Q9 model is used, similar to all calculations carried out in [6,7,27,30,31,33]. On open boundaries, a one-sided 4th-order compact method is used to derive the first derivatives. For ease of reference, other numerical details and the M_∞/Re_∞ and Pr_∞ values assumed for the vortex- and thermal-scattering problems are given in Tables 1 and 2.

IV. Acoustic Waves Scattering by a Zero-Circulation Vortex

A schematic showing the incoming acoustic wave, the vortex, and the coordinate system in a 2-D formulation is given in Fig. 1a. Plane sound waves with small amplitude and a wavelength $\hat{\lambda}$ propagate in the positive x direction in a uniform, homogeneous fluid toward a line vortex with zero circulation lying along the z axis, which is normal to

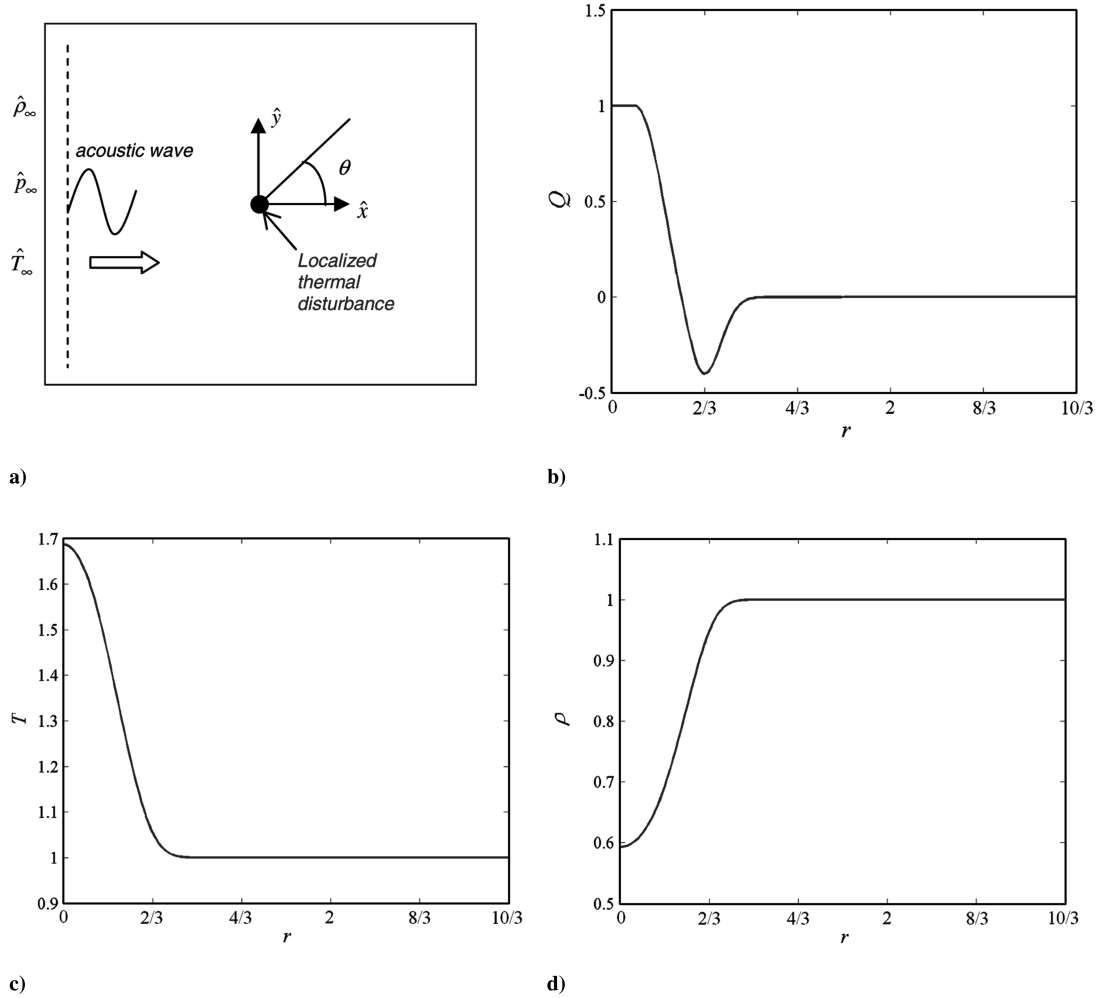

Fig. 8 Sketch of the acoustic-scattering problem and the corresponding Q, T, and ρ distributions of the thermal disturbance.

the xy plane. This specification allows the vortex to approximate a rigid body of very small size. Therefore, when the sound waves impinge on the vortex, it will oscillate and the induced flow will move with the continuous plane waves, and sound radiation will result. In spite of this oscillation, the net circulation $\hat{\Gamma}$ around the vortex is zero. This picture is qualitatively correct, at least for large $\hat{\lambda}$ incoming waves. It should be noted that this flow has a $M_\infty \ll 1$, a consequence of weak incoming waves that are supposed to have little or no disturbance on the vortex (i.e., the vortex remains a rigid body).

The strength of the scattering field is very weak; at least 10^{-2} smaller than the incoming waves, which are themselves of acoustic strength. Thus, the scattering field is always submerged inside the background of the continuous incoming waves. A finite computational domain measuring $2\hat{h} \times (2\hat{l} + \hat{\lambda})$, with the vortex located at the origin of this domain, is used to carry out the calculations (Fig. 1b). To resolve the scattered waves correctly, truly nonreflecting computational boundaries are required for both DAS and FDLBM simulations. For DAS, the boundary treatment method follows the suggestions of [5–7], where an absorbing region D_I is invoked for the inlet boundary and a region D_O is assumed for the outlet boundary, while a zero-order extrapolation of u, v, p, and so forth, is assumed for the top and bottom boundary. For the FDLBM, the same absorbing region as that used in the DAS calculation is invoked for the left and right boundary, but it is used to absorb the fluctuations of f [27]. Grid refinement tests for DAS scheme have been carried out by Leung et al. [39] and their findings are adopted for the vortex scattering simulation. For the upper and lower boundary, a zero-order extrapolation for f is used. Details are given in Table 1.

Vorticity distribution plays an important role in this scattering problem. According to the theoretical derivation of [4], it was found that the scattered field was related to the Fourier transform of the vorticity distribution. In the present case, an incoming pressure pulse impinging on a zero-circulation vortex is calculated using FDLBM and DAS. The integration of vorticity over the whole volume should vanish, which is essentially the consequence of a zero-circulation vortex. The definition for a zero-circulation vortex or Taylor vortex is given by [4,40]

$$\hat{\omega}(r) = \hat{\omega}_0[2 - r^2]\exp\left[\frac{1 - r^2}{2}\right] \tag{17}$$

where $\hat{\omega}_0$ is the characteristic vorticity strength and $r = \hat{r}/\hat{L}$ is the dimensionless radial coordinate, with $\hat{L}$ the characteristic length of

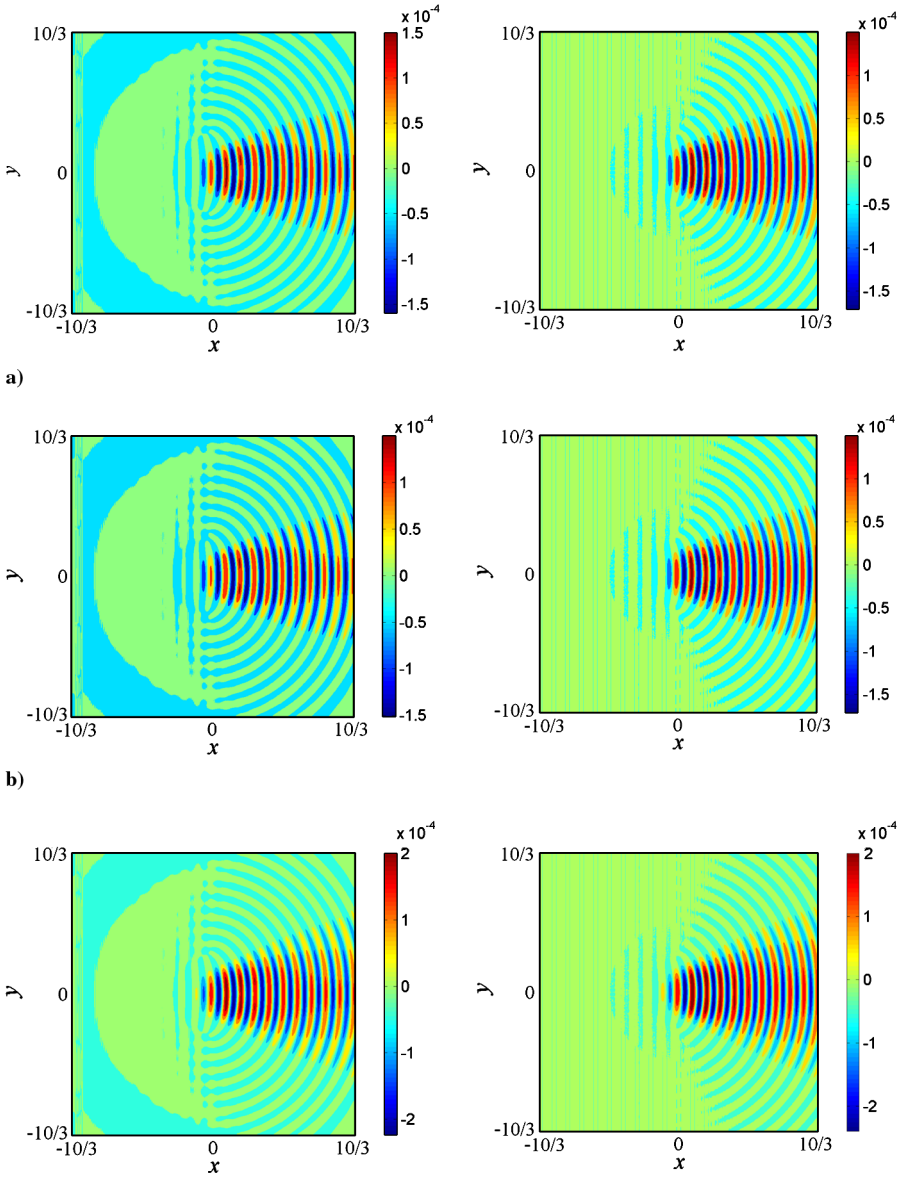

Fig. 9 2-D contours of a) p_s, b) ρ_s, and c) T_s for the $\lambda = 1/3$ thermal-scattering case. The left-hand column represents FDLBM, and the right-hand column represents DAS.

the obstacle. In the numerical computation, the pressure pulse and the vortex are initialized by

$$p_w = p_\infty\left[1 + \varepsilon_p \sin\left(\frac{2\pi c}{\lambda}t\right)\right] \tag{18a}$$

$$\rho = \rho_\infty, \qquad u = u_\infty + \varepsilon y \exp(x_2)$$
$$v = v_\infty - \varepsilon x \exp(x_2), \qquad p = p_\infty \tag{18b}$$

where $x_2 = -\ell_n 2(x^2 + y^2)/0.4^2$, the mean field density and pressure are given by $\rho_\infty = 1$ and $p_\infty = 1/\gamma$, and the amplitudes $\epsilon_p = 10^{-4}$ and $\varepsilon = 10^{-1}$ are assumed. The incoming waves are excited once the Taylor vortex is initialized at the center of the domain. Immediately, a scattered field is created and is submerged inside the incoming wave field. This scattered field can be obtained by subtracting two solutions, that is, $\rho_s = \rho_{v+w} - \rho_w$, where the subscript $(v + w)$ indicates the solution of the vortex plus incoming waves, and w indicates the incoming waves alone. Altogether two $\lambda = \hat{\lambda}/\hat{L}$ cases are attempted using both FDLBM and DAS. In general, these cases can be classified by the Helmholz number $H_n = 2\pi\hat{L}/\hat{\lambda}$. By choosing $H_n = 4\pi$ and 0.8π, the two cases are specified by $\lambda = 0.5$ and $\lambda = 2.5$, respectively. In view of the reliability of the DAS calculation [4], it is used as benchmark to validate the FDLBM simulation. Because the vortex has zero circulation, Γ calculated for each λ should be identically zero; otherwise, there will be a lift force acting on the vortex and this will affect the calculated scattered field pattern.

A. Vortex Scattering for $\lambda = 0.5$ (Wentzel–Kramers–Brillouin Limit)

The 2-D contours of p_s, ρ_s, and T_s for this case are plotted in Fig. 2. Both DAS and FDLBM solutions are shown (the left-hand column is the FDLBM solution and the right-hand column is DAS solution). It can be seen that the scattered pattern is quite symmetric and a shadow is clearly seen at the back of the vortex. This illustrates the preferred direction of scattering of the acoustic waves. To show the symmetric directivity character more clearly, the absolute values of the amplitudes of the p_s, ρ_s, and T_s fluctuations along the circumferential direction at $\hat{r}/\hat{\lambda} = 5$ for both FDLBM and DAS calculations are plotted in Fig. 3 for comparison. These absolute values are denoted by $|P|$, $|\rho|$, and $|T|$, respectively. The plots clearly show the locations of the peaks at approximately $\theta = \pm\pi/6$ (where θ is measured positive counterclockwise) and the DAS calculated peaks are slightly less than those given by the FDLBM simulation. On the other hand, the modified LBM calculation of [28] showed asymmetry about $\theta = 0$; the peak on the negative θ side is lower than that on the positive θ side. Further, note that the disturbance field calculated by the FDLBM is essentially zero beyond $\pm\pi/2$; however, it is not quite zero for the modified LBM result in [28]. It is also not zero for the current DAS result at $\pi/2$; a peak, albeit very small, appears in the plots of $|P|$, $|\rho|$, and $|T|$. This could be a consequence of interference derived from reflected waves from the top boundary. In other words, the DAS top and bottom boundary condition settings do not perform as well as those specified for the FDLBM. For the sake of brevity, the distributions of p_s and T_s along r for different θ will not be shown here; instead they will be compared with the $\lambda = 2.5$ case later. As for the behavior of the elements of P'_{ij}, they are not shown because their behavior is quite similar to those calculated for the $\lambda = 2.5$ case (which are shown in the following section).

The time required for each successful numerical simulation in an IBM server pSeries 670 is detailed in Table 1. It can be seen that the DAS simulation is more than 11 times faster than the FDLBM calculation. This is not a fair comparison because the simulations were carried out using different Δt for FDLBM and DAS. Further, the Runge–Kutta scheme is 2nd-order accurate for FDLBM and it is 4th-order accurate for DAS. Given that Δt for FDLBM is 2 orders of magnitude smaller, a ten-fold increase in computing time is not surprising; besides, the Δt chosen is based on the CFL conditions and has not been optimized to reach the stability limit.

For this case, grid refinement computation has also been carried out by reducing the grid size (Δx and Δy) by one half. The resulting norm two error between the fine and coarse grid result is of the order 10^{-12}, which is negligible compared with the scattered wave amplitude (10^{-6}). The norm two error between the coarse grid and the DAS result is of the order 10^{-7}. In other words, the norm two error between the two different grids of the FDLBM simulation is smaller than that between the FDLBM and the DAS. The current (coarser) grid is more than adequate to resolve the scattered field of this $\lambda = 0.5$ acoustic-scattering problem; therefore, it is the grid size of choice for all subsequent FDLBM simulations.

B. Vortex Scattering for $\lambda = 2.5$ (Born Limit)

The FDLBM and DAS results for this case are given in Figs. 4 and 5. Contour plots of p_s, ρ_s, and T_s are shown in Fig. 4, and the directivity figures are depicted in Fig. 5. For this case, the scattered wave spreads out in all directions and no sharp-edged shadow is observed (Fig. 4). Also, the scattered wave pattern is symmetric about the x axis. This result is reproduced by the FDLBM simulation (Figs. 4 and 5). The FDLBM results are essentially symmetric about $\theta = 0$, the peak values are occurring in pairs at locations $\theta = \pm\pi/4$

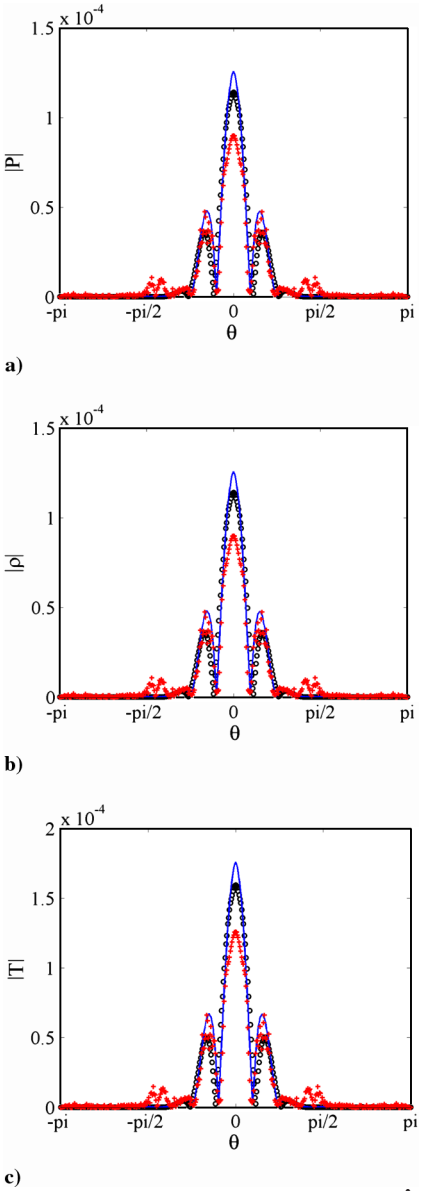

Fig. 10 Directivity plots of a) p_s, b) ρ_s, and c) T_s at $\hat{r}/\hat{\lambda} = 5$ for the $\lambda = 1/3$ thermal-scattering case. The solid line represents analysis, the circles represent FDLBM, and + represents the gas-kinetic scheme.

and $\pm 3\pi/4$, and $|P| = 0$, $|\rho| = 0$, and $|T| = 0$ occur at locations $\theta = 0, \pm\pi/2$, and $\pm\pi$. Therefore, these observations lend evidence to the observed symmetry of the distributions of p_s, ρ_s, and T_s.

On the other hand, a close examination of the DAS plots of p_s, ρ_s, and T_s at $\hat{r}/\hat{\lambda} = 2$ reveals that these plots are not exactly symmetric (Fig. 4). The asymmetry can be clearly discerned from the directivity plots shown in Fig. 5. Firstly, the magnitudes of the peaks at approximately $\theta = \pm\pi/4$ and $\pm 3\pi/4$ are all different. Secondly, the directivity plots are not symmetric about $\theta = 0$. This asymmetry can be seen by examining the θ locations where $|P| = 0$, $|\rho| = 0$, and $|T| = 0$, and by the base values of the directivity patterns at $|P| = 0$, $|\rho| = 0$, and $|T| = 0$. If the directivity plots were symmetric, they should occur at $\theta = 0$, $\pm\pi/2$, and $\pm\pi$, and the base values are all equal to $\pi/2$, just as the FDLBM results show (Fig. 5). The DAS results show that $|P| = 0$, $|\rho| = 0$, and $|T| = 0$ do not occur at $\theta = \pm\pi/4$ and $\pm 3\pi/4$, and the base values of the directivity patterns are all different. These results suggest that vorticity is present in the flow field, and the source of this rotation might be caused by the existence of a very small circulation Γ resulting from the numerical simulation.

Various differences between the DAS and FDLBM numerical calculations could contribute to the asymmetry observed. Chief among them is the choice of the time step ($\Delta t = 0.0001$ for FDLBM and $\Delta t = 0.01$ for DAS), and its impact on the accuracy of the calculated Γ and on the directivity pattern. Firstly, Γ is estimated from the FDLBM and DAS results. For the $\lambda = 0.5$ (WKB limit) case, $\Gamma \cong 0$ is obtained for both FDLBM and DAS simulations. On the other hand, for the $\lambda = 2.5$ (Born limit) case, DAS result yields a $\Gamma = 6.257 \times 10^{-10}$, whereas FDLBM simulation gives a $\Gamma = 1.701 \times 10^{-10}$. The calculated Γ is negligibly small (even though the DAS result is about 4 times that deduced from FDLBM); therefore, it is not likely that the estimated Γ is large enough to produce a finite displacement of the vortex that could lead to an asymmetric behavior of the directivity pattern. The next step is to check the effect of Δt on the calculated Γ. Further calculations with $\Delta t = 0.005$ and 0.05 have been carried out with other parameters specified the same as those given in Table 1. These results reveal that the calculated directivity patterns for $\Delta t = 0.005$, 0.05, and 0.01, respectively, are essentially identical and the difference in the estimated Γ is again negligibly small. It appears that the cause for the observed asymmetric behavior

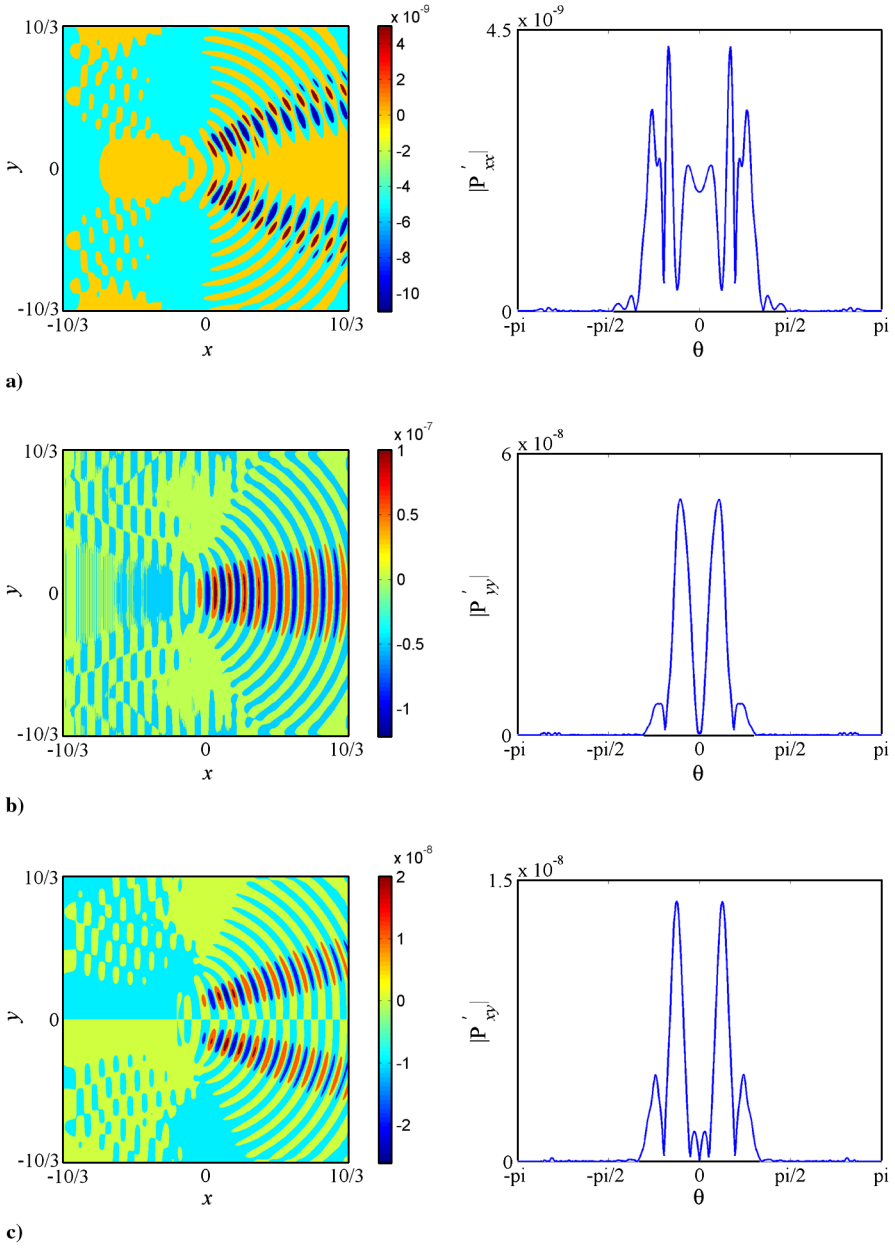

Fig. 11 The FDLBM simulated scattered field of P'_{ij} for the $\lambda = 1/3$ thermal-scattering case: a) P'_{xx}; b) P'_{yy}, and c) P'_{xy}. The left-hand column represents 2-D contours, and the right-hand column represents directivity at $\hat{r}/\hat{\lambda} = 5$.

of the DAS result for the Born limit case is not known. One thing is certain though; the asymmetry is not likely caused by differences in Γ and numerical errors.

The distributions of p_s and T_s along r for five different values of θ varying from 0 to $\pi/2$ for the two λ cases are plotted in Fig. 6 for comparison. It can be seen that the distributions of $|P|$ and $|T|$ are essentially identical for all θ shown for the $\lambda = 0.5$ case (Fig. 6a), but there are slight differences for the $\lambda = 2.5$ case (Fig. 6b). This further illustrates that the vortex has been displaced slightly from the coordinate origin in the DAS simulation.

Only the 2-D contours and directivity plots of P'_{xx}, P'_{yy}, and P'_{xy} for the $\lambda = 2.5$ case are shown in Fig. 7. Those for the $\lambda = 0.5$ case are very similar; therefore, for the sake of brevity, they are not shown. The contour patterns and magnitudes of P'_{xx} and P'_{yy} are similar and, to a great extent, so are their directivity plots (see Figs. 7a and 7b). On the other hand, the contour plot and magnitude of P'_{xy} are different from those shown for P'_{xx} and P'_{yy} (it is at least 1 order of magnitude smaller), and so is its directivity behavior (Fig. 7c). The role played by P'_{ij} in the FDLBM simulation can be gleaned from a comparison of the behavior and magnitude of P'_{ij} with those of τ_{ij}, and the importance of the elements of P'_{ij} and τ_{ij} in determining the coefficients Bxx_1, Byy_1, and Bxy_2 given in Eqs. (13f–13h). Similar contour behavior is observed for the elements P'_{xx} and P'_{yy}, and τ_{xx} and τ_{yy}, respectively; so is the contour behavior for P'_{xy} and τ_{xy}. Further, their magnitudes are essentially the same. This implies that the elements of P'_{ij} play a role similar to the elements of τ_{ij}; therefore, the elements of P'_{ij} are just as important as those of τ_{ij} in determining the f^{eq}_{α} distribution.

For this $\lambda = 2.5$ case, the wall clock running time for FDLBM is only about 4 times larger than that for DAS. It should be pointed out that the same Δt was used for both λ investigated, that is, in both cases Δt for FDLBM is 2 orders of magnitude smaller than that for DAS. The Δt was assigned in a conservative manner; it was not optimized to reach the stability limit. Rather, it was chosen to give maximum accuracy for the FDLBM results. Together, these two FDLBM simulations show that significant improvement in computing time is possible. Furthermore, due to the simplicity of the core algorithm of the LBM and its all-local nature, abundant research on performance evaluation and optimization of LBM for large-scale computer architecture has been conducted [41,42]. Parallel computing could facilitate further reduction in wall clock running time for the FDLBM.

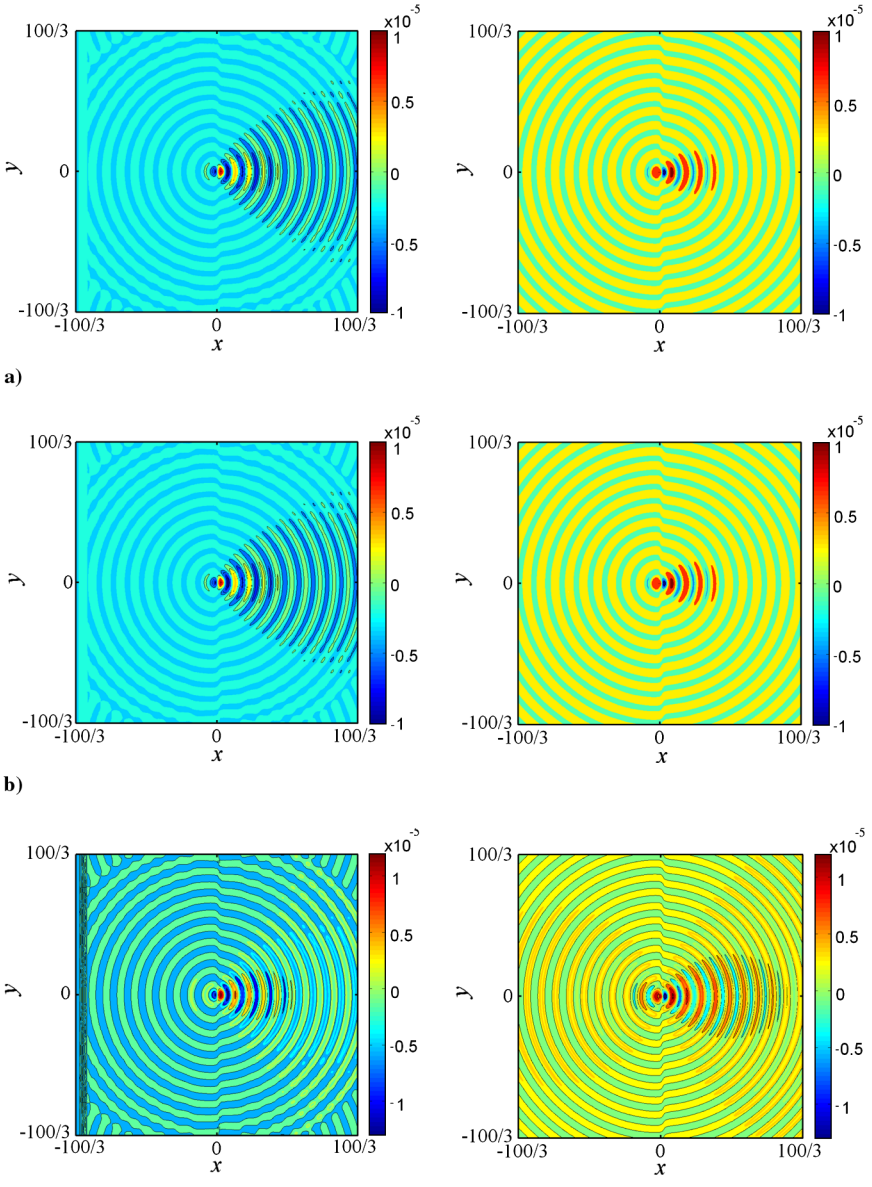

Fig. 12 2-D contours of a) p_s, b) ρ_s, and c) T_s for the $\lambda = 10/3$ thermal-scattering case. The left-hand column represents FDLBM, and the right-hand columns represents analysis.

V. Acoustic Waves Scattering by a Localized Thermal Disturbance

Analogous to the vortex-scattering case, the thermal-scattering problem is defined by incoming acoustic waves impinging on a thermal disturbance (Fig. 8a). The thermal disturbance is constructed from a weak temperature distribution such that the net heat gain/loss is zero, much like the zero-circulation vortex. Consequently, the thermal disturbance is stationary with respect to time. The reason for this choice of thermal disturbance is that if the net heat gain/loss is not zero, there will be a flow of thermal energy from the disturbance even in the absence of the incoming acoustic waves, and this further complicates the analysis of the acoustic/aerodynamic interaction. However, according to Chu [43], the zero heat gain/loss type of weak thermal disturbance renders the analysis of the acoustic/aerodynamic interaction in a viscous compressible thermal flow more manageable. Thus, this problem is amenable to a linear analysis [20], and provides a benchmark to validate any numerical simulations of thermal scattering.

According to Kam et al. [20], the temperature distribution within an axisymmetric heat source in a quiescent fluid can be solved by invoking an inviscid fluid assumption and a linearized treatment of the governing Euler equations. Under these assumptions, the governing equations are reduced to,

$$C\frac{1}{r}\frac{\mathrm{d}}{\mathrm{d}r}\left\{r\frac{\mathrm{d}[T(r)]}{\mathrm{d}r}\right\} = -Q(r) \tag{19a}$$

where $r = \hat{r}/\hat{L}$ is the dimensionless radial coordinate, $Q(r)$ is the source strength, and $C = \hat{\kappa}/\hat{\rho}_\infty \hat{a}_\infty \hat{L}(\hat{c}_p)_\infty(\gamma - 1)$. Equation (19a) will admit to a regular solution if $Q(r)$ is specified by the condition

$$\int_0^\infty Q(r) r\,\mathrm{d}r = 0 \tag{19b}$$

and the distribution of $Q(r)$ is given by [20]

$$Q(r) = Q_1(r) = 1, \quad \text{for } r \le r_1 \tag{20a}$$

$$Q(r) = Q_2(r) = C_1 + (1 - C_1)e^{-\left(\frac{r-r_1}{b_1}\right)^2}, \quad \text{for } r_1 \le r \le r_2 \tag{20b}$$

$$Q(r) = Q_3(r) = C_2\left(1 - e^{\left(\frac{r_3-r_2}{b_2}\right)^2 - \left(\frac{r-r_3}{b_2}\right)^2}\right), \quad \text{for } r_2 \le r \le r_3 \tag{20c}$$

$$Q(r) = Q_4(r) = C_3 e^{\left(\frac{r_3-r_2}{b_2}\right)^2 - \left(\frac{r-r_3}{b_3}\right)^2}, \quad \text{for } r_3 \le r \tag{20d}$$

Here $r_1 = 1/6$, $r_2 = 1/2$, $r_3 = 2/3$, $b_1 = 1.0$, $b_2 \approx 0.6401$, $b_3 = 0.5$, $C_1 = e^{-1}/(e^{-1} - 1) \approx 0.5820$, $C_2 \approx 0.4769$, and $C_3 \approx 0.2178$. To visualize sound scattering by this axisymmetric heat source, $Q(r)$ is assumed bounded at $r = 1.0$. Once $Q(r)$ is known, T can be evaluated by solving Eq. (19a) and ρ is obtained from the perfect gas state equation. For reference, the distributions of Q, T, and ρ are shown in Fig. 8b–8d, respectively. Once the thermal disturbance is defined, the acoustic field can be derived using the linearized Euler equation approach and the assumption that the disturbance is not affected by the incident acoustic wave. Therefore, this approach cannot be used to resolve the acoustic-thermal interaction between the incident wave and the thermal disturbance. Nevertheless, the analytical solution still yields a fundamental solution for scattering [20] that will serve as benchmark for numerical simulation of the same problem where the acoustic-thermal interaction could be accounted for by solving the full set of NS equations instead of the linearized Euler equations.

Again, two cases are attempted; the WKB limit where the incoming wave has small λ and the Born limit where the incoming wave has relatively large λ (due to computing facility limitation, simulation with very large λ cannot be performed). These two cases are classified by the Helmholtz number $H_n = 2\pi\hat{L}/\hat{\lambda}$, which is an indication of the compactness of acoustic scattering. The two cases chosen for investigation have $H_n = 6\pi$ and 0.6π, corresponding to $\lambda = 1/3$ (WKB limit) and $10/3$ (Born limit), respectively. Different values of H_n will give rise to different directivity patterns; therefore, the two limiting cases chosen will lead to totally different directivity patterns. The thermal disturbance is assumed to be bounded at $r = 1.0$, $\hat{L} = 3$. Therefore, by choosing the computational domain as tabulated in Table 2, there are 10 waves within the domain for each limit considered. As later computations show, this is sufficient to allow the acoustic field to be resolved accurately. All calculations, be it FDLBM, the gas-kinetic scheme [20–22], or theoretical analysis, are carried out using the same computational domain. Because theoretical solutions are available for all λ, there is no need to perform a DAS computation of this problem. Instead, the present FDLBM simulations are compared with the theoretical results for the WKB and Born limit cases, and the gas-kinetic scheme is used to calculate the $\lambda = 1/3$ case only because its simulation of the $\lambda = 10/3$ case is not satisfactory [20]. Key results of these two cases are selected to illustrate the acoustic features without duplication compared with those presented in [20], and are plotted in Figs. 9–14 for comparison.

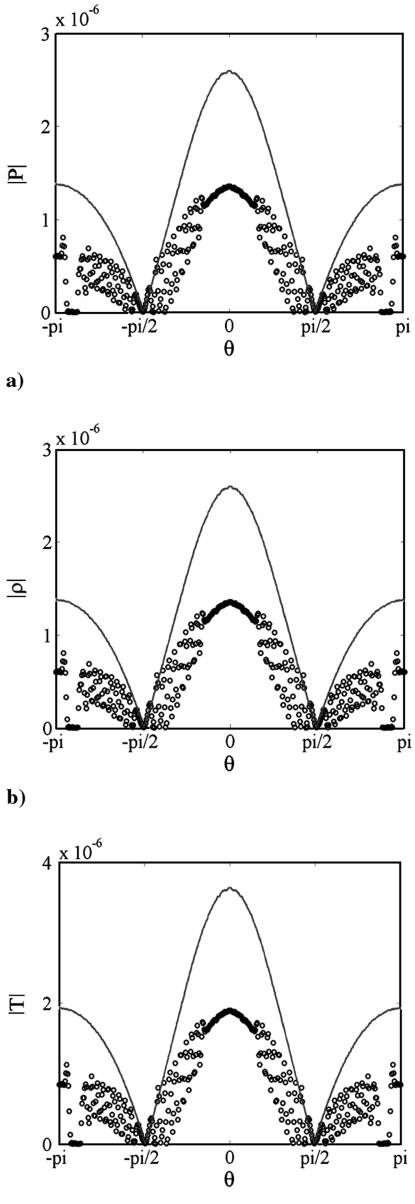

Fig. 13 Directivity plots of a) p_s, b) ρ_s, and c) T_s at $\hat{r}/\hat{\lambda} = 10$ for the $\lambda = 10/3$ thermal-scattering case. The circles represents FDLBM, and the solid line represents DAS.

A. Thermal-Scattering for $\lambda = 1/3$ (WKB limit)

Three different calculations of this case have been carried out; they are the theoretical analysis, the FDLBM, and the gas-kinetic scheme. It should be pointed out that the FDLBM is solved using a 6th-order finite difference scheme (Table 2) whereas the finite volume scheme used in the gas-kinetic scheme is only 3rd-order accurate. The numerical details are specified in Table 2. A detailed comparison between the gas-kinetic and theoretical results have already been made in [20]; therefore, the present comparison is made to highlight the pros and cons of the FDLBM simulations compared with analysis. For this case, as a result of the interaction of the scattered wave with the undisturbed incoming wave behind the obstacle (the thermal disturbance), a sharp-edged shadow is formed behind the obstacle. This was clearly shown in [20] for both gas-kinetic and analytical results. A comparison of the contour plots of the FDLBM and analytical results for the scattered pressure p_s, density ρ_s, and temperature T_s are shown in Fig. 9. It is clear that the scattered patterns for these two simulations are very similar.

The similarity can be further illustrated by comparing the directivity plots of p_s, ρ_s, and T_s at $\hat{r}/\hat{\lambda} = 5$ for the three different calculations (Fig. 10). The analytical result is symmetric about the x axis with a peak occurring at $\theta = 0$ and two other peaks at $\theta = \pm\pi/6$ and $\pm \sim \pi/3$. The FDLBM result yields the same behavior. On the other hand, the gas-kinetic result gives rise to two more additional peaks at $\theta = \pm \sim 4\pi/9$ and $\pm\pi/2$. In addition, two other differences between the analytical, FDLBM, and gas-kinetic results can be observed from Fig. 10. The first is that the directivity plots are very clean for the theoretical and FDLBM results, but high-frequency oscillations are evident in the gas-kinetic simulation. The appearance of high-frequency oscillations and the additional peaks is an indication that the nonreflecting boundary condition (Reimann invariants) invoked for the gas-kinetic scheme is not very effective. Otherwise, reflected waves would not be present to interact with the incoming and scattered waves to produce these differences between the gas-kinetic scheme and the analytical and FDLBM results. The second is the peak values reached at the locations $\theta = 0, \pm\pi/6$, and $\pm \sim \pi/3$. Because the theoretical solution is obtained from the linearized Euler equations, dissipation effect is absent in the formulation. The FDLBM and the gas-kinetic scheme solve the full set of NS equations; therefore, dissipative behavior would lead to lower peak values at these locations. The FDLBM gives lower peaks at these θ locations compared with analysis, a result consistent with

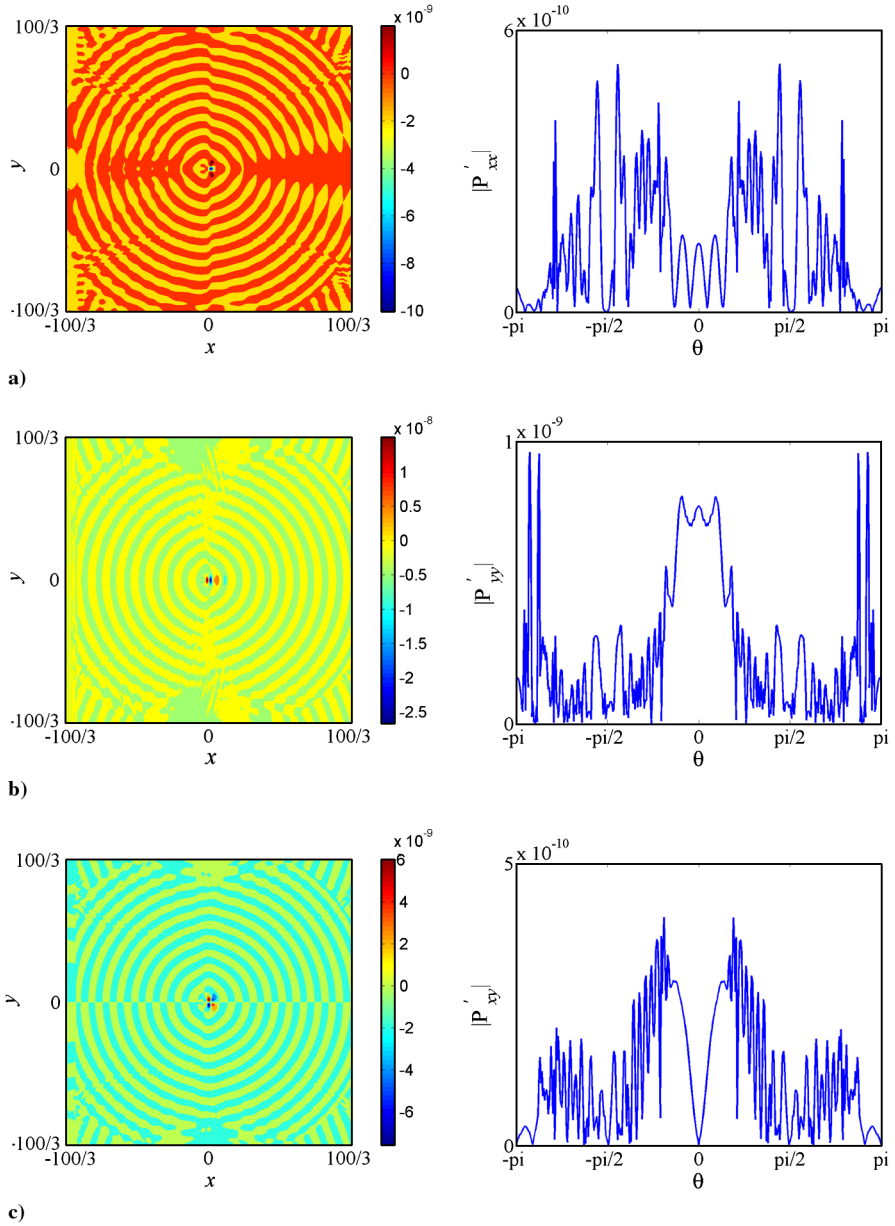

Fig. 14 The FDLBM simulated scattered field of P'_{ij} for the $\lambda = 10/3$ thermal-scattering case: a) P'_{xx}, b) P'_{yy}, and c) P'_{xy}. The left-hand column represents 2-D contours, and the right-hand column represents directivity at $\hat{r}/\hat{\lambda} = 5$.

the NS equations treatment. However, the gas-kinetic scheme yields inconsistent results, a peak much lower than the FDLBM value at $\theta = 0$, but the same peak values at $\theta = \pm\pi/6$ and $\pm \sim \pi/3$. One reason could be due to the accuracy of the numerical scheme used, 6th-order finite difference for the analysis and FDLBM, 3rd-order finite volume for the gas-kinetic scheme. A less accurate numerical scheme could lead to greater diffusion from $\theta = 0$ toward larger values of θ. This could partially explain the lower peak value at $\theta = 0$ and more or less the same peak values compared with analysis at $\theta = \pm\pi/6$ and $\pm \sim \pi/3$.

The behavior of P'_{ij} is plotted in Fig. 11 to illustrate the role it plays in the FDLBM simulation. In a 2-D problem, only three elements of P'_{ij} are nonzero. Therefore, the contour and directivity plots (at $\hat{r}/\hat{\lambda} = 5$) of P'_{xx}, P'_{yy}, and P'_{xy} are shown in Fig. 11. The directivity plots of P'_{xx}, P'_{yy}, and P'_{xy} are not similar to those shown for $|P|$, $|\rho|$, and $|T|$ in Fig. 10. At $\theta = 0$, a minimum is registered rather than a peak value as that shown in Fig. 10. The peak magnitudes are at least four orders of magnitude less than those shown in Fig. 10. The contour plots of P'_{xx}, P'_{yy}, and P'_{xy} essentially follow those shown in Fig. 9 for $\hat{p}$, $\hat{\rho}$, and $\hat{T}$, but the magnitudes are 3–5 orders smaller. The magnitude of the P'_{yy} contours is at least 1 order of magnitude larger than those of P'_{xx} and P'_{xy}. These values are small compared with p, but they are essentially the same as the corresponding elements of τ_{ij}, thus playing a role that is just as important as that played by τ_{ij} [see Eqs. (13f–13h)] in determining the coefficients Bxx_1, Byy_1, and Bxy_2, and the eventual behavior of f_α^{eq}.

B. Thermal Scattering for $\lambda = 10/3$ (Born Limit)

In this case, $\hat{L} = 0.3\hat{\lambda}$ and it can be regarded as the long wavelength or Born limit case. Only two simulations were carried out for this case, an FDLBM and a theoretical calculation. The 3rd-order accurate gas-kinetic scheme has been used to simulate this case and reported in [20]. The results were not good compared with analysis. The reasons could be traced to the inappropriateness of the Reimann invariants invoked at the open boundary and the less than accurate numerical scheme. Therefore, no attempt is made to compare the FDLBM with the gas-kinetic scheme result.

The scattered waves spread out in all directions as reflected waves for very large λ. Because the interfering waves can be considered negligible, no sharp-edged shadow is expected in the scattered field. The 2-D contours of p_s, ρ_s, and T_s for both calculations are plotted in Fig. 12 for comparison. The scattered waves are spread out in all directions, more so in the analysis than in the FDLBM result. A sharp-edged shadow is still noticeable in both calculations, though much larger for the FDLBM p and ρ result. This means that the wavelength of the incoming waves is not large enough; it is only 3.33 times larger than $\hat{\lambda}$. The directivity plots of p_s, ρ_s, and T_s at $\hat{r}/\hat{\lambda} = 10$ for both calculations are shown in Fig. 13 for comparison. The long wavelength combined with the viscous dissipation effect gives rise to a much lower peak (about half the theoretical value) at $\theta = 0$ and $\pm\pi$ for the FDLBM result, and more high-frequency oscillations. However, the symmetric behavior is still predicted by FDLBM, and there is no phase shift noted in the FDLBM simulation. This implies that the heat gain/loss of the thermal disturbance is indeed zero as calculated by FDLBM. Finally, the 2-D contour and directivity plots of P'_{ij} are shown in Fig. 14. The 2-D contours and directivity plots are 1 order of magnitude smaller than the corresponding plots in the $\lambda = 1/3$ case. The contour behavior is similar to those of p_s, ρ_s, and T_s. The directivity plots show more high-frequency oscillations compared with the $\lambda = 1/3$ case. Even then, symmetric behavior is preserved.

VI. Conclusions

An FDLBM has been proposed for the numerical simulation of acoustics scattering by an obstacle. The FDLBM is based on a modeled lattice Boltzmann equation with an alternative equilibrium particle distribution function that is capable of recovering the Navier–Stokes equations correct to order Kn with no restrictions on M_∞. However, it requires the specification of Re_∞ and Pr_∞, much like the solution of the Navier–Stokes equations using any finite difference scheme. Furthermore, the FDLBM is a 6th-order accurate scheme and is able to simulate acoustic disturbances stably and correctly.

Scattering by two different obstacles was investigated; one given by a zero-circulation vortex, another represented by a localized thermal disturbance with zero heat gain/loss. As such, the obstacles behave like rigid body. Depending on the ratio (λ) of the incoming wavelength to the characteristic dimension of the obstacle, two limiting cases of scattering will result. If the ratio is very small it is classified as the WKB limit; if it is very large it is designated as the Born limit. Consequently, the scattering pattern is greatly influenced by λ. The scattered wave is the difference between two waves, one resulting from the interaction of the incoming acoustic wave with the obstacle, and the other the undisturbed acoustic wave. Consequently, its magnitude is very small and is difficult to simulate accurately. These cases, therefore, serve as critical benchmarks to test the validity and extent of the FDLBM.

The FDLBM simulations of the vortex-scattering case were compared with solution of the Navier–Stokes equations using a DAS technique and the gas-kinetic scheme. The FDLBM and the DAS technique employed a 6th-order finite difference compact scheme and the results thus obtained are essentially identical for the WKB limit. However, the gas-kinetic scheme is only 3rd-order accurate; therefore, the comparison is not as good. Asymmetric behavior of the scattering field for the Born limit was predicted by DAS, but not by FDLBM. The reason could be traced to a very small circulation around the vortex calculated by the DAS technique. As a result, the symmetry of scattering is affected by the very small lift acting on the vortex. This is not the case with the FDLBM; the calculated circulation is 4 times smaller than that deduced from DAS. The gas-kinetic scheme prediction, on the other hand, is contaminated by numerical noise.

The linearized thermal-scattering problem admits to a theoretical solution; therefore, the FDLBM simulation of this case is compared with the theoretical result. The FDLBM result is in good agreement with analysis for the WKB limit. The only difference is in the prediction of the scattering peak located at the symmetry line. Because the analysis is based on the linearized Euler equations, viscous dissipation is absent. This explains the noted difference in the calculated peak values. The difference in the predicted peak values increases for the Born limit case, but the symmetric behavior of acoustic scattering is still replicated by the FDLBM. The FDLBM simulations, in general, fair better than the gas-kinetic scheme results.

Acknowledgments

Funding support from the Hong Kong Polytechnic University is gratefully acknowledged; E. W. S. Kam and S. C. Fu for Ph.D. studentship awarded them in the course of their studies, and R. C. K. Leung for grants A-PA5U and A-PA9Y awarded him. R. M. C. So acknowledges support received from the National Science Foundation grant CBET-0854411 awarded to New Mexico State University.

References

[1] Colonius, T., and Lele, S. K., "Computational Aeroacoustics: Progress on Nonlinear Problems of Sound Generation," *Progress in Aerospace Sciences*, Vol. 40, No. 6, 2004, pp. 345–416. doi:10.1016/j.paerosci.2004.09.001

[2] Colonius, T., Lele, S. K., and Moin, P., "Boundary Conditions for Direct Computation of Aerodynamic Sound Generation," *AIAA Journal*, Vol. 31, No. 9, 1993, pp. 1574–1582. doi:10.2514/3.11817

[3] Lele, S. K., "Compact Finite Schemes with Spectral-Like Resolution," *Journal of Computational Physics*, Vol. 103, No. 1, 1992, pp. 16–42. doi:10.1016/0021-9991(92)90324-R

[4] Colonius, T., Lele, S. K., and Moin, P., "The Scattering of Sound Waves by a Vortex: Numerical Simulations and analytical solutions," *Journal*

of Fluid Mechanics, Vol. 260, 1994, pp. 271–298.
doi:10.1017/S0022112094003514

[5] Leung, R. C. K., Li, X. M., and So, R. M. C., "A Comparative Study of Non-Reflecting Condition for One-Step Numerical Simulation of Duct Aero-Acoustics," *AIAA Journal*, Vol. 44, No. 3, 2006, pp. 664–667.
doi:10.2514/1.18215

[6] Li, X. M., Leung, R. C. K., and So, R. M. C., "One-Step Aeroacoustics Simulation Using Lattice Boltzmann Method," *AIAA Journal*, Vol. 44, No. 1, 2006, pp. 78–89.
doi:10.2514/1.15993

[7] Li, X. M., So, R. M. C., and Leung, R. C. K., "Propagation Speed, Internal Energy and Direct Aeroacoustics Simulation Using Lattice Boltzmann Method," *AIAA Journal*, Vol. 44, No. 12, 2006, pp. 2896–2903.
doi:10.2514/1.18933

[8] Georges, T. M., "Acoustic Ray Paths through a Model Vortex with a Viscous Core," *The Journal of Acoustical Society of America*, Vol. 51, No. 1b, 1972, pp. 206–209.
doi:10.1121/1.1912831

[9] Müller, E. A., and Matschat, K. R., "The Scattering of Sound by a Single Vortex and by Turbulence," Air Force Office of Scientific Research, Technical Rept. TN59-337, AD 213658, Göttingen, Germany, 1959.

[10] Ferziger, J. H., "Low-Frequency Acoustic Scattering from a Trailing Vortex," *The Journal of Acoustical Society of America*, Vol. 56, No. 6, 1974, pp. 1705–1707.
doi:10.1121/1.1903502

[11] O'Shea, S., "Sound Scattering by a Potential Vortex," *Journal of Sound and Vibration*, Vol. 43, No. 11, 1975, pp. 109–116.
doi:10.1016/0022-460X(75)90209-6

[12] Howe, M. S., "Contributions to the Theory of Aerodynamic Sound, with Application to Excess Jet Noise and the Theory of the Flute," *Journal of Fluid Mechanics*, Vol. 71, No. 4, 1975, pp. 625–673.
doi:10.1017/S0022112075002777

[13] Candel, S. M., "Numerical Solution of Wave Scattering Problems in the Parabolic Approximation," *Journal of Fluid Mechanics*, Vol. 90, No. 3, 1979, pp. 465–507.
doi:10.1017/S0022112079002354

[14] Ford, R., and Llewellyn Smith, S. G., "Scattering of Acoustic Waves by a Vortex," *Journal of Fluid Mechanics*, Vol. 386, No. , 1999, pp. 305–328.
doi:10.1017/S0022112099004371

[15] Mawardi, O. K., "Aero-Thermoacoustics, The Generation of Sound by Turbulence and by Heat Processes," *Reports on Progress in Physics*, Vol. 19, 1956, pp. 156–187.
doi:10.1088/0034-4885/19/1/305

[16] Bass, H. E., "Absorption of Sound by Air: High Temperature Prediction," *The Journal of Acoustical Society of America*, Vol. 69, No. 1, 1981, pp. 124–138.
doi:10.1121/1.385356

[17] Trilling, L., "On Thermally Induced Sound Fields," *The Journal of the Acoustical Society of America*, Vol. 27, No. 3, 1955, pp. 425–431.
doi:10.1121/1.1907920

[18] Reinschke, J., Möhring, W., and Obermeier, F., "Scattering of Sound Waves by a Cylindrical Vortex: a Semi-Analytical Theory," *Journal of Fluid Mechanics*, Vol. 333, 1997, pp. 273–299.
doi:10.1017/S0022112096004211

[19] Farouk, B., Oran, E. S., and Fusegi, T., "Numerical Study of Thermoacoustic Waves in an Enclosure," *Physics of Fluids*, Vol. 12, No. 5, 2000, pp. 1052–1061.
doi:10.1063/1.870360

[20] Kam, E. W. S., So, R. M. C., and Leung, R. C. K., "Acoustic Scattering by a Localized Thermal Disturbance," *AIAA Journal*, Vol. 47, No. 9, 2009, pp. 2039–2052.

[21] Su, M., Xu, K., and Ghidaoui, M. S., "Low-Speed Flow Simulation by the Gas-Kinetic Scheme," *Journal of Computational Physics*, Vol. 150, 1999, pp. 17–39.
doi:10.1006/jcph.1998.6162

[22] Xu, K., and He, X. Y., "Lattice Boltzmann Method and Gas-Kinetic BGK Scheme in the Low-Mach Number Viscous Flow Simulations," *Journal of Computational Physics*, Vol. 190, No. 1, 2003, pp. 100–117.
doi:10.1016/S0021-9991(03)00255-9

[23] Buick, J. M., Greated, C. A., and Campbell, D. M., "Lattice BGK Simulation of Sound Waves," *Europhysics Letters*, Vol. 43, No. 3, 1998, pp. 235–240.
doi:10.1209/epl/i1998-00346-7

[24] Buick, J. M., Buckley, C. L., Greated, C. A., and Gilbert, J., "Lattice Boltzmann BGK Simulation of Nonlinear Sound Waves: the Development of a Shock Front," *Journal of Physics A: Mathematical and General*, Vol. 33, No. 21, 2000, pp. 3917–3928.
doi:10.1088/0305-4470/33/21/305

[25] Tsutahara, M., Kataoka, T., Takada, N., Kang, H. K., and Kurita, M., "Simulations of Compressible Flows by Using the Lattice Boltzmann and the Finite Difference Lattice Boltzmann Methods," *Computational Fluid Dynamics Journal*, Vol. 11, No. 1, 2002, pp. 486–493.

[26] Ricot, D., Maillard, V., and Bailly, C., "Numerical Simulation of Unsteady Cavity Flow Using Lattice Boltzmann Method," AIAA Paper No. AIAA 2002-2532, 2002.

[27] Kam, E. W. S., So, R. M. C., and Leung, R. C. K., "Lattice Boltzmann Method Simulation of Aeroacoustics and Nonreflecting Boundary Conditions," *AIAA Journal*, Vol. 45, No. 7, 2007, pp. 1703–1712.
doi:10.2514/1.27632

[28] Li, X. M., "Computational Aeroacoustics Using Lattice Boltzmann Method," Ph.D. thesis, Department of Mechanical Engineering, The Hong Kong Polytechnic Univ., Hong Kong, 2006.

[29] Kam, E. W. S., "Prediction of Noise Generation by Using Modeled Boltzmann Equation," Ph.D. thesis, Dept. of Mechanical Engineering, The Hong Kong Polytechnic Univ., Hong Kong, 2008.

[30] Fu, S. C., So, R. M. C., and Leung, R. C. K., "Modeled Boltzmann Equation and Its Application to Direct Aeroacoustics Simulation," *AIAA Journal*, Vol. 46, No. 7, 2008, pp. 1651–1662.
doi:10.2514/1.33250

[31] So, R. M. C., Leung, R. C. K., and Fu, S. C., "Modeled Boltzmann Equation and Its Application to Shock Capturing Simulation," *AIAA Journal*, Vol. 46, No. 12, 2008, pp. 3038–3048.
doi:10.2514/1.35332

[32] Watari, M., "Finite Difference Lattice Boltzmann Method with Arbitrary Specific Heat Ratio Applicable to Supersonic Flow Simulations," *Physica A: Statistical Mechanics and Its Applications (Amsterdam)*, Vol. 382, No. 2, 2007, pp. 502–522.
doi:10.1016/j.physa.2007.03.037

[33] So, R. M. C., Fu, S. C., and Leung, R. C. K., "Finite Difference Lattice Boltzmann Method for Compressible Thermal Fluids," *AIAA Journal* (submitted for publication).

[34] Bhatnagar, P., Gross, E. P., and Krook, M., "A Model for Collision Processes in Gases, 1 Small Amplitude Processes in Charged and Neutral One-Component Systems," *Physical Review*, Vol. 94, No. 3, 1954, pp. 511–525.
doi:10.1103/PhysRev.94.511

[35] Lele, S. K., *Direct Numerical Simulations of Compressible Turbulent Flows: Fundamentals and Applications, Chap. 7 of Transition, Turbulence and Combustion Modeling*, edited by A. Hanifi, P. H. Alfredsson, A. V. Johansson, and D. S. Hennigson, Kluwer Academic, Norwell, MA, 1998, pp. 424–429, Chap. 7.

[36] Toro, E. F., *Riemann Solvers and Numerical Methods for Fluid Dynamics: A Practical Introduction*, 2nd ed., Springer–Verlag, New York, 1999, Chap. 15.

[37] Fu, S. C., Leung, W. W. F., and So, R. M. C., "A Lattice Boltzmann Method Based Numerical Scheme for Micro-Channel Flows," *Proceedings of IMECE08 2008, ASME International Mechanical Engineering Congress and Exposition*, IMECE Paper No. 2008–67654, Boston, MA, 2008; also to appear in *Journal of Fluids Engineering*, Vol. 131, 2009.

[38] Chapman, S., and Cowling, T. G., *The Mathematical Theory of Non-uniform Gases*, Cambridge Univ. Press, Cambridge, England, 1939.

[39] Leung, R. C. K., So, R. M. C., Kam, E. W. S., and Li, X. M., "An Attempt to Calculate Acoustic Directivity Using LBM," AIAA, Paper No. 2006–2574, Reston, VA, 2006.

[40] Taylor, G. I., "On the Dissipation of Eddies," Aeronautical Research Committee, Reports and Memoranda 598, 1918.

[41] Wellein, G., Lammers, P., Hager, G., Donath, S., and Zeiser, T., "Towards Optimal Performance for Lattice Boltzmann Applications on Terascale Computers," *Parallel Computational Fluid Dynamics: Theory and Applications*, edited by A. Deane, G. Brenner, A. Ecer, D. Emerson, J. McDonough, J. Periaux, A. Satofuka, and D. Tromeur–Dervout, Proceedings of the 2005 International Conference on Parallel Computational Fluid Dynamics, College Park, MD, May 24–27 2005, pp. 31–40.

[42] Wellein, G., Zeiser, T., Hager, G., and Donath, S., "On the Single Processor Performance for Simple Lattice Boltzmann Kernels," *Computers and Fluids*, Vol. 35, No. 8–9, 2006, pp. 910–919.
doi:10.1016/j.compfluid.2005.02.008

[43] Chu, B. T., "On the Energy Transfer to Small Disturbances in Fluid Flow (Part I)," *Acta Mechanica*, Vol. 1, No. 3, 1965, pp. 215–234.
doi:10.1007/BF01387235

C. Bailly
Associate Editor